Journal of Cluster Science (2025) 36:70
https://doi.org/10.1007/s10876-025-02770-w

ORIGINAL PAPER

Synthesis of Zinc Oxide Nanoparticles and Their Potential Application in the Detection of Latent Fingerprints

Betty Flores[1] · Maribel Guzman[2] · Rolf Grieseler[1] · Aransselly Quiroz[1] · Loic Malet[3] · Stephane Godet[3]

Received: 11 October 2024 / Accepted: 20 January 2025 / Published online: 19 March 2025

Abstract

Zinc oxide in nanometric dimensions, thanks to its optical properties, is an oxide of great interest for its potential use as a revealing agent for latent fingerprints. In this article we present the synthesis and characterization of ZnO nanoparticles obtained by two methods and it uses in revealing of latent fingerprints on non-porous surfaces. The nanoparticles synthetized present an atomic Zn:O ratio of 0.99 and 1.15 when precipitation and combustion in solution method were used, respectively. Both samples show a hexagonal arrangement (wurtzite) according to the X-ray diffraction and Raman spectra. Raman results show a shift at 439 cm^{-1} corresponding to the E_2 (high) mode of the ZnO crystalline hexagonal wurtzite structure. Transmission electron microscopy images show that nanoparticles with smaller average diameters are obtained by chemical precipitation (17.2 ± 10.8 nm) than combustion in solution (73.4 ± 6.0 nm). Samples presented a narrow band gap of 3.69 and 3.59 eV, values higher than that reported for the bulk material (3.37 eV). The photoluminescence spectrum showed a characteristic ultraviolet emission peak around 387 nm and green emissions peaks from ZnO when excitation wavelength of 325 and 488 nm were experiment, respectively. Finally, ZnO nanoparticles were used to reveal latent fingerprints on non-porous surfaces using a 325 nm laser. Fingerprint development is better on black glass surface when using precipitated ZnO. However, Fingerprints are better observed in aluminum foil when ZnO obtained by combustion in solution is applied. The results show that it is possible to use ZnO nanoparticles obtained by both methods as latent fingerprint revealing agents.

Keywords Latent fingerprints · Nanoparticles · Precipitation · Photoluminescence · Zinc oxide

Introduction

For decades the identification of people has been used through the development and study of fingerprints. The use of this technique, together with the decoding of DNA, is one of the greatest discoveries in forensic sciences. When a crime is carried out, it is important to identify the individual who committed it by collecting evidence at the scene, in order to find the culprit.

The most important evidence that can be collected at a crime scene are deoxyribonucleic acid (DNA) traces and latent fingerprints (LFPs) [1]. However, contamination or loss of DNA and LFP prior to collection could affect the analysis of this evidence [2, 3]. For this reason, forensic science has evolved in recent years, improving methods and techniques for the scientific research of important material (evidence) related to a criminal act [4]. In crime scene investigation, LFPs are the first evidence that must be collected and revealed for the identification of a suspect [4–8]. Forensic science presents many methods to detect and improve the acquisition and development of LFPs [9–18]. The simplest conventional method for developing LFPs at a crime scene is to apply a fine powder to fingerprints left on non-porous surfaces [15–19]. After removing excess of fine dust, particles adhering to the ridges of the print are examined to find unique patterns that allow an individual to be identified. However, this current method has still limitations such as low sensitivity, little selectivity and poor contrast [20, 21]. To eliminate or reduce these problems, advances in nanotechnology have allowed the use of a certain class of

✉ Maribel Guzman
mguzman@pucp.edu.pe

[1] Department of Sciences, Pontifical Catholic University of Peru, Avenida Universitaria 1801, Lima, Peru

[2] Department of Engineering, Pontifical Catholic University of Peru, Avenida Universitaria 1801, Lima, Peru

[3] 4MAT, Université Libre de Bruxelles, CP194/03, avenue F.D. Roosevelt 50, 1050 Bruxelles, Belgium

nanoparticles whose luminescent characteristics allow better development of LFPs [20–23].

There are many doped or undoped metal oxides nanoparticles that have a variety of applications extending from antibacterial, biomedical, environmental, photocatalytic and of course LFP revealing. Among these compounds we can mention the un-doped oxides of aluminum (Al_2O_3) [22, 24], cerium (CeO_2) [25], copper (CuO) [24], iron (Fe_2O_3, Fe_3O_4) [20, 25–27], rare earth elements (EuO, Y_2O_3) [20, 23, 28, 29], silicon (SiO_2) [20, 22, 23, 30–32], tin (SnO) [33], titanium (TiO_2, Ti_2O_3) [20, 23, 25, 34–36], and zinc (ZnO) [22, 23, 25, 33, 37–48]. On the other hand, to improve the optical properties of these oxides, researchers have explored the possibility of incorporating doping elements into their structure [49, 50]. For doped oxides we can mention doping agents such as cobalt–nickel (Co–Ni:TiO_2) [51], copper–zinc–cobalt (Cu–Zn–Co:Fe_2O_3) [52], chromium (Cr:CoO) [53] and Yttrium (Y:CoO, Y:ZnO) [45, 53].

Alternatively, taking advantage of their interesting optical properties, zinc oxide nanoparticles (ZnO NPs) seem to be an interesting alternative to be used as revealing LFPs [43, 54–58]. In fact, if the ZnO structure presents crystallographic defects, it is possible to observe visible luminescence around 580 nm by exciting the sample with ultraviolet light (300–400 nm). Due to this phenomenon, it is possible to detect and observe LFP in the green range of the visible light spectrum [59]. However, research on the use of undoped ZnO nanoparticles to reveal LFPs on non-porous surfaces such as aluminum [37, 40, 60], stainless steel [42] and clear glass has been limited [25, 37, 39, 42, 44]. And in the case of dark glass, they are almost non-existent.

Many methods for obtaining ZnO nanostructures can be found in the literature [48, 61]. Nevertheless, combustion in solution [39, 62–64] and chemical precipitation [38, 65–69] are the easiest methods to carry out because they do not require sophisticated equipment. In precipitation process, the synthesis parameters such as type of reagents, temperature, pH and reaction time can influence the morphology and size of the nanoparticles. While oxidizing agents can do the same in combustion in solution synthesis. The size and morphology of ZnO Nps can influence their optical properties and therefore their potential application as fingerprint developers. In the case of precipitation method, Pramanik et al. [40] and Verma et al. [42] have proposed a synthesis using zinc acetate and zinc chloride respectively; but zinc nitrate has not been reported as a reagent to synthesize ZnO Nps that have been tested in LFPs development. While Deepthi et al. [39] has reported the synthesis of ZnO Nps by combustion in solution using Barbituric acid, 1,3-Dimethylbarbituric acid and 2-thiobarbituric acid as oxidants. There are no reports of the use of glycine in this type of synthesis to obtain ZnO Nps that were subsequently used to develop LFPs. In order to evaluate whether there is any influence on the optical properties of the synthesized ZnO Nps, zinc nitrate was proposed as a source of zinc ions and glycine as an oxidizing agent for the proposed synthesis methods.

This article summarizes the results of the synthesis and characterization of ZnO NPs obtained by two synthesis methods: chemical precipitation in aqueous medium and combustion in solution. As well as their evaluation in the development of LFPs on different non-porous surfaces (aluminum, stainless steel, clear glass and dark glass).

Experimental Section

Materials Used

Experimental materials and apparatus are supplied in Supporting Information. The chemicals used in this study are presented in Table 1.

Synthesis of ZnO NPs

For chemical precipitation, solutions of zinc nitrate (0.02 M) and sodium hydroxide (0.4 M) were used [70]. 25 ml of solution containing the zinc ions was placed in a beaker where a stoichiometric amount (K^+/Zn^{+2}, 1:1) of potassium nitrate (0.1 M) was added. 25 ml of sodium hydroxide solution was dropped at 1 mL/s, maintaining the pH and temperature reaction at 11 and 60 °C under stirring (400 rpm), respectively. During this time, the formation of ZnO Nps

Table 1 List of chemical reagents with chemical formula, purity, and suppliers, used as raw materials

Chemical Reagents	Chemical formula	Molecular mass (g/mol)	Purity (%)	Suppliers
Acetone	$CH_3(CO)CH_3$	58.08	≥ 99.5%	Honeywell Riedel–de Haen
Ethanol	C_2H_5OH	46.068	99.5	J.T. Baker
Glycine	$NH_2CH_2CO_2H$	75.067	99	Riedel-de Haen AG Seelze-Hannover
Potassium nitrate	KNO_3	101.1032	99.5	Scharlau
Sodium hydroxide	NaOH	39.997	≥ 99	Merck
Zinc nitrate	$Zn(NO_3)_2.6H_2O$	297.48	≥ 98	Sigma-Aldrich (Darmstadt, Germany)

takes place through two parallel processes: nucleation and continuous growth of nuclei [67, 71]:

$$Zn^{2+}_{(aq)} + 2(OH)^{-}_{(aq)} \leftrightarrows Zn(OH)_{2(s)} \quad (1)$$

$$Zn(OH)_{2(s)} + 2(OH)^{-}_{(aq)} \leftrightarrows Zn(OH)^{2-}_{4(aq)} \quad (2)$$

$$Zn(OH)^{2-}_{4(aq)} \leftrightarrows ZnO_{(s)} + 2H_2O_{(l)} + 2OH^{-}_{(aq)} \quad (3)$$

Once the reaction (3) was completed (around 2 h), the colloids were centrifuged at 6500 rpm using a microcentrifuge (Eppendorf 5804, Germany). The nanoparticles were washed two times with MilliQ-water (Millipore, Germany). The product obtained was gently dried in an oven at 60 °C for 24 h.

For combustion in solution, an amount of zinc nitrate (~ 5 g) and glycine (~ 3 g) were dissolved in 20 ml of water under continuous magnetic stirring [39]. The roles of zinc nitrate and glycine are to be a source of zinc, and fuel and oxidant, respectively. The viscous mixture was then placed in a porcelain crucible and placed in a muffle preheated to 500 °C. After approximately 2 min, combustion takes place, giving way to the formation of ZnO nanostructures [72, 73]:

$$2Zn^{2+}_{(aq)} + 4CH_2(NH_2)CO^{-}_{2(aq)} + 9O_{2(g)} \xrightarrow{\Delta} 2ZnO_{(s)} + 8CO_{2(g)} + 8H_2O_{(g)} + 2N_{2(g)} \quad (4)$$

Once combustion is completed, the crucible is removed from the muffle. The ZnO Nps obtained were gently placed in a vial for subsequent characterization.

Characterization Techniques

The chemical composition was determined by Scanning Electron Microscopy-Energy Dispersive Spectroscopy (SEM-EDS). The crystallographic nature was evaluated by X-ray diffraction (XRD); additional information on the chemical structure and crystallinity is provided by selected area electron diffraction (SAED) and Raman spectroscopy. The average nanoparticle size as well as their morphology are assessed by transmission electron microscopy (TEM). While the optical properties were evaluated by ultraviolet–visible (UV–Vis) and photoluminescence spectroscopy (PL).

Collection and Development of LFPs

LFPs were provided by a single female participant. To avoid any interference due to dust, she gently washed her hands with soap and dried them with a hand dryer. Next the volunteer placed and pressed her index finger during 5 s on previously cleaned non-porous surfaces (aluminum foil, black glass, stainless steel and clear glass). These surfaces were selected because they are frequently found at crime scenes. The surfaces were cleaned with a swab moistened with acetone/ethanol. The surfaces were then dried in a desiccator, to be placed on a Petrie dish to prevent dust adsorption on their surface. The ZnO Nps were gently applied on the surfaces using a fine commercial brush No. 2230 from Loreal following the procedure proposed by Choi et al. [74]. After, LFPs were developed by irradiation with ultraviolet light (325 nm) (Fig. 1). Images of the LFPs sprinkled with ZnO Nps on different surfaces were obtained using the 40× optical zoom in full high definition (HD) of a digital camera (Canon Power Shot SX410 IS). For these tests, a commercial ZnO particles sample as a reference material was used.

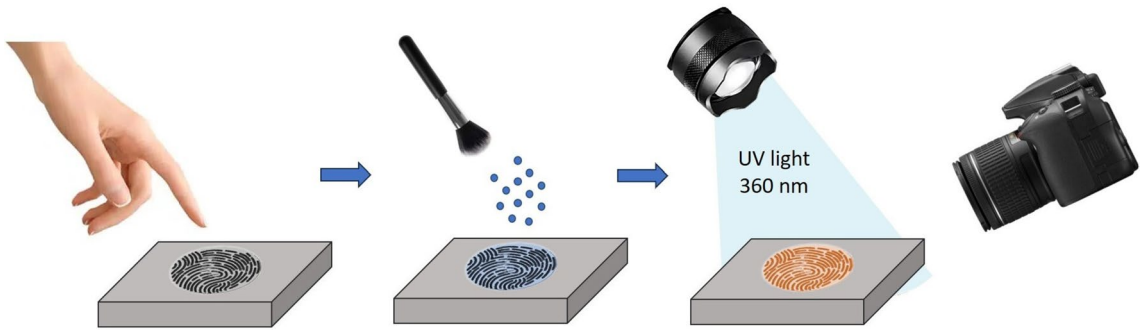

Fig. 1 Methodology used to impregnate non-porous surfaces containing latent finger prints with ZnO nanoparticles; and its subsequent development with UV light (360 nm)

Results and Discussion

SEM-EDS Analysis of ZnO Nps

The EDS spectra and the elemental compositions of oxygen and zinc of the ZnO nanoparticles are presented in Fig. 2. For the three samples, the K and L emission peaks of zinc ($K_\alpha = 8.630$ keV and $L_\alpha = 1.012$ keV) and oxygen ($K_\alpha = 0.525$ keV) are observed. Any peaks of contaminating element are not observed. The C emission peak ($K_\alpha = 0.277$ keV) is due to the sample holder tape.

The Zn:O atomic ratio calculated from the EDS analysis varied from 0.99 and 1.36. For reference material, ZnO nanoparticles obtained by precipitation and combustion in solution were 1.36 [75, 76], 0.99 [77–79] and 1.15 [64], respectively. In view of the theoretical value of the Zn:O ratio = 1, we can affirm that with method-2 the ZnO Nps present an oxygen deficit during its formation process (Eq. 4). The elemental mapping of each sample shows a homogeneous distribution and overlap images of zinc and oxygen atoms, evidencing the formation of ZnO (Fig. 2).

XRD Analysis of ZnO Nps

Figure 3a, c, e show the XRD spectra of ZnO NPs samples. The identified (100), (002), (101), (102), (110), (103) and (112) diffraction plane families coincide with the hexagonal phase of wurtzite-type zinc oxide (Joint Committee on Powder Diffraction Standards, JCPDS card no. 36-1451) [64, 76, 79–86]. Likewise, no additional diffraction peaks belonging to another compound formed are observed. Therefore, we can confirm that ZnO has been formed by both methods. Furthermore, selected-area electron diffraction pattern allows us to confirm the wurtzite-like hexagonal crystal structure of ZnO Nps (Fig. 3b, d, f). The SAED micrographs show the bright spots indicating the crystalline nature of the reference material and the material prepared by both synthesis routes [87, 88]. The bright spots, which coincide with an almost circular pattern of concentric rings, reflect the polycrystalline nature of the ZnO nanoparticles [89–95]. The concentric circles were indexed to the (100), (101), (102), (110), (103) and (112) diffraction planes corresponding to the JCPDS card 36-145 for the ZnO wurtzite structure [40, 60, 85, 87–89, 91, 96, 97]. According to the results obtained with the selected area electron diffraction (SAED) pattern, the d-spacing values of 2.81, 2.48, 1.91, 1.63, 1.46 and 1.36 Å correspond to the hexagonal phase of ZnO [66, 86–88]. Similar SAED were previously reported by others authors [60, 66, 71, 85, 86, 89].

The XRD data of the samples were subjected to Rietveld refinement using Topas program, employing the background function of Chebyschev [98, 99]. The input data to a refinement include the space group ($P6_3mc$), atomic positions, site occupancies (0.33333 and 0.66667), and lattices parameters (a = 3.2490 and c = 5.2060) [100]. All Rietveld refinement factors such as, goodness of fit (χ^2), and various R-factors such as Bragg factor (R_B), expected factor (R_{exp}), profile factor (R_p) and weighted profile factor (R_{wp}) are summarized in the Table 2. The χ^2 is around 2.0 for the commercial sample and ZnO Nps obtained by combustion in solution revealing high quality of the fit. We can observe that an excellent agreement was found between the experimental spectra and the calculated values [101, 102]. During Rietveld refinement we have considered that size broadening has only the Lorentzian component [103], potential profile broadening due to strain and defects are not considered. The estimated size of the nanocrystal was determined by Rietveld refinement [98]. The results are presented in Table 2.

Raman Analysis of ZnO Nps

Raman spectra of ZnO NPs measured under 633 nm excitation are show in Fig. 4. Raman spectra show a main peak at 439 cm^{-1} and small peaks at 334 and 391 cm^{-1}. The second-order Raman mode, E_2(high) characteristic of the hexagonal structure of wurtzite-type ZnO is observed at 439 cm^{-1} [40, 104, 105]. Small peaks situated at 202 and 583 cm^{-1} are assigned to the second-order vibrations [104], and the E_1 of longitudinal optical (LO) second-order Raman scattering [106–108], respectively. It is further observed that the second-order Raman process is assigned to the peak that appears around 330 cm^{-1} [40, 79, 104, 105, 109]. It is also observed that transverse optical (TO) modes with A_1 symmetry appear at 391 cm^{-1} [105, 108]. Then, all bands in the Raman spectra can be assigned to wurtzite ZnO [105]. A summary with all vibrational modes is presented in Table 3.

TEM Analysis of ZnO Nps

The Fig. 5 shows the TEM micrographs of ZnO NPs. It can be noted that smaller nanoparticles were synthesized by method-1 ($\phi = 17.2$ nm ± 10.8 nm) [110–112], compared to method-2 ($\phi = 73.4$ nm ± 6.0 nm) [112]. The ZnO NPs obtained have different particle size distributions. With method-1, a size distribution that varies from 5.0 to 62.8 nm is obtained (Fig. 5a), while with method-2 the particles range between 66.5 nm to 86.5 nm (Fig. 5b). Method-1 produces smaller ZnO Nps but with a larger size distribution. The ZnO Nps obtained are smaller than those obtained by Pramanik et al. [40] and Verma et al. [42] with the same methodology. In the case of method-2, the nanoparticles obtained are larger but present better control of the particle size (narrower size distribution). In this case the ZnO Nps

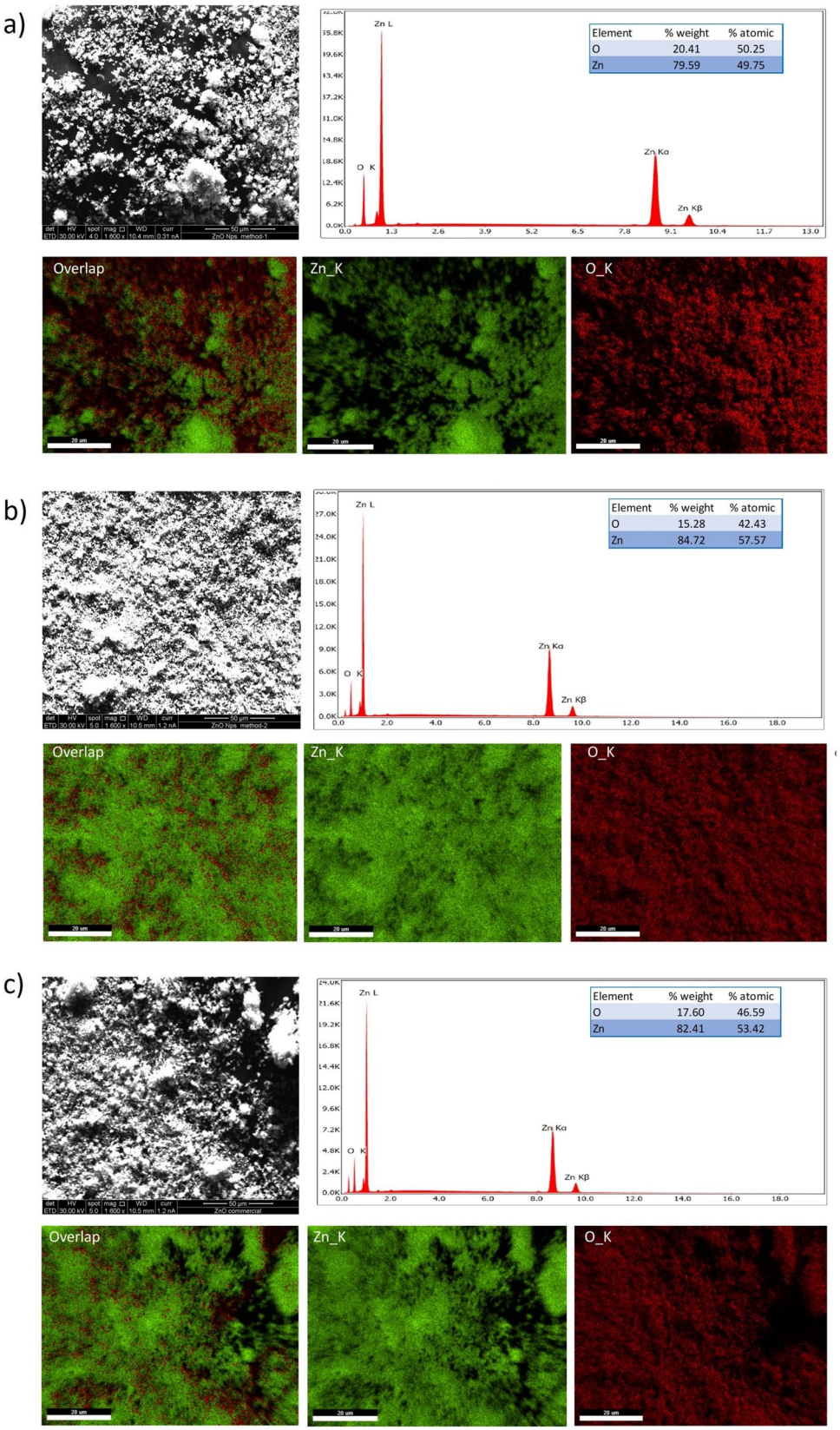

Fig. 2 SEM figures, EDS spectra, chemical composition and mapping with the element (Zn and O) distribution of ZnO nanoparticles obtained by **a** chemical precipitation, **b** combustion in solution, and **c** commercial sample

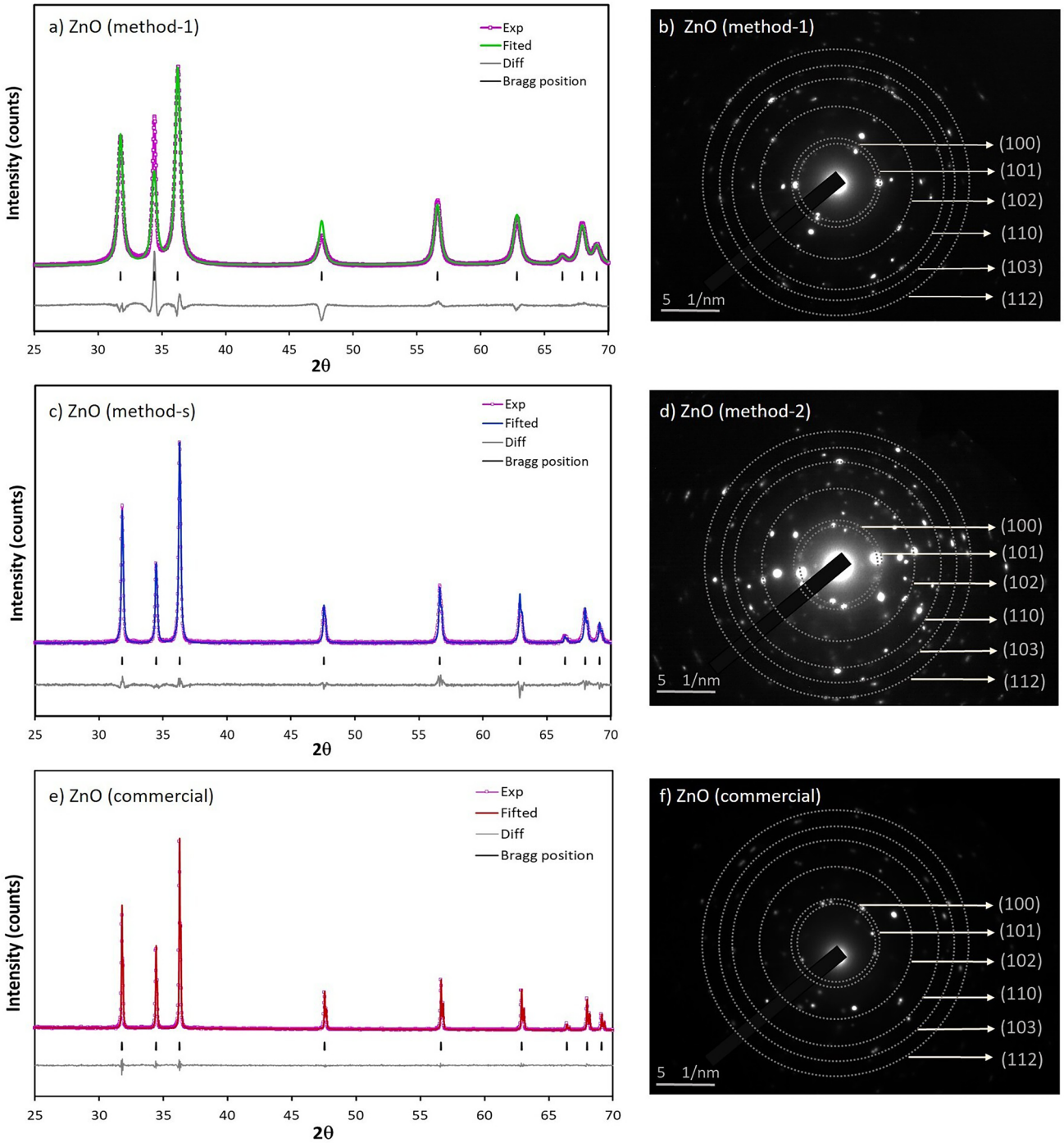

Fig. 3 XRD spectra with peaks, crystal lattices and selected area (electron) diffraction (SAED) of ZnO nanoparticles obtained by **a**, **d** chemical precipitation, **b**, **e** combustion in solution, and **c**, **f** commercial sample. Spectra were obtained over the range 2θ = 25–70° using a step size of 0.03° and counting time of 10 seconds per step

obtained are larger than those obtained by Deepthi et al. [39]. Finally, Fig. 5c shows that the commercial sample is composed of larger particles with a size distribution from 48 to 390 nm and an average diameter of 184.4 nm ± 82.0 nm (Fig. 5c). Regarding morphology, it is observed that the ZnO NPs obtained by method-1 are poorly defined, some of them are hemispherical; while those obtained by method-2 are almost square. This can be explained because the formation of ZnO Nps by method-1 is carried out by a nucleation process and a continuous growth of nuclei. In the case of

Table 2 Average diameter, crystallite size and Rietveld refined structural parameters of ZnO nanoparticles samples obtained by different synthesis methods

Method applied	Mean diameter[a] (nm)	Crystallite size[b] (nm)	R_B	R_{exp}	R_p	R_{wp}	χ^2
Chemical precipitation	17.2 ± 10.8	23.7	3.030	2.47	6.75	10.33	4.18
Combustion in Solution	73.4 ± 6.0	81.1	2.603	3.72	4.29	5.73	1.54
Commercial	184.4 ± 82.0	258.4	0.573	4.70	4.34	5.48	1.17

[a]Obtained by TEM

[b]Calculated using the Rietveld refinement

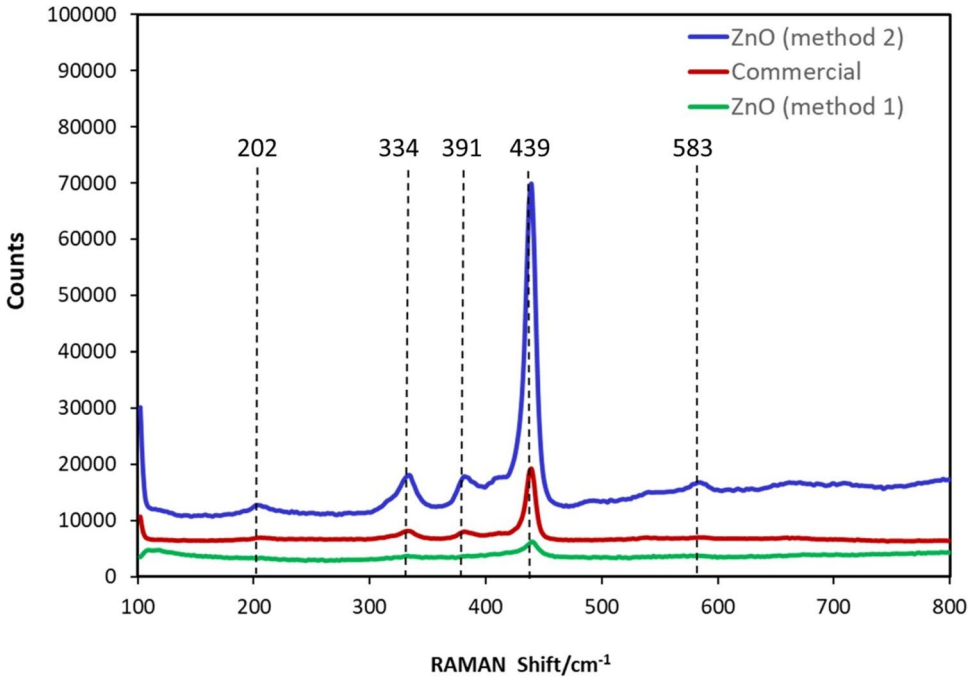

Fig. 4 Raman spectra recorded at an excitation wavelength of 633 nm for ZnO nanoparticles synthesized by chemical precipitation, combustion in solution, and commercial sample. Spectra were acquired for 10 s with 3 accumulations using a laser power was kept at 29.3 μW

method-2, ZnO Nps are obtained in a single step [72]. Since the method-2 reaction is extremely fast, the growth process takes place in the solid residue of combustion [73]. Therefore, slightly larger particles should be attributed to aggregation or superposition of small particles [113]. Table 2 summarizes the crystallite size values obtained by Rietveld refinement and the average diameter sizes calculated from TEM images [98].

UV–Vis Analysis of ZnO Nps

The UV–Vis spectra for the reference sample and the prepared ZnO samples are presented in Fig. 6. The reference sample presents a small peak at 379 nm (3.27 eV) [114–116]; while the prepared ZnO nanoparticles by method-1 and method-2 show a small absorption at 372 nm (3.34 eV) [66, 115, 117, 118] and 373 nm (3.32 eV) [119], respectively. The UV emission band, which is well known as the near band-edge emission (NBE) band, is located around 380 nm [40, 120, 121]. This emission is generated by the free-exciton recombination and the visible region known to be deep-level emission appearing due to the structural defects and impurities in the structures [90]. Other absorption peaks have not been observed. Similar aspects have been reported previously [25, 40, 65, 121]. This would indicate a blue shift respect to bulk ZnO (λ = 368 nm; 3.37 eV) and this could be attributed to the effects of confinement [122], because the prepared samples are made up of nanoparticles.

The absorbance measured by UV–Vis was used to determine the E_g value using the Tauc's formula, $(\alpha h\nu)^{1/n} = A(h\nu - E_g)$ [121]. Where α is the absorption coefficient, h is Planck's constant, ν the frequency of the incident photons, A is a constant, n is the transition probability (n = 1/2 for a direct transition semiconductor) and E_g is the band gap energy [66, 76, 123–125].

Comparing the two synthesis methods, it was determined that E_g decreases with increasing crystallite size [116]. Indeed, the bandgap value of the ZnO nanoparticles systematically decreased (red shift) from 3.688 to 3.591 eV. This coincides with the increase in the size of

Table 3 Vibration modes observed in the Raman spectra of ZnO nanoparticle samples

Vibrational mode	Raman shift (cm^{-1})		
	Chemical reduction	Combustion in solution	Commercial sample
Inactive Raman mode, E_2 (low)	197	202	206
E_2 (High), E_2 (Low)	332	334	332
A_1 (TO)	395	391	391
E_2 (High)	439	439	439
E_1 (LO)	582	583	583

Fig. 5 TEM images, particle size distribution and mean diameter of ZnO nanoparticles obtained by **a** chemical precipitation, **b** combustion in solution, and **c** commercial sample. An ethanolic solution containing a small amount of nanopowder was deposited on a carbon-coated TEM copper grid. TEM images were obtained using a Philips CM20-Ultra Twin microscope operating at 200 kV (Philips; Eindhoven, The Netherlands)

the crystallites [125]. The reference sample shows a band-gap of 3.464 eV, a lower value expected due to its larger particle size.

Photoluminescence Analysis of ZnO Nps

In a ZnO structure there can be three different types of intrinsic defects: vacancy, interstitial and antisite [126]. In this case, we have the zinc vacancies (V_{Zn}), oxygen vacancies (V_o), zinc interstitial (Zn_i), oxygen interstitial (O_i), zinc antisite (Zn_O) and antisite of oxygen (O_{Zn}). The optical properties of ZnO nanostructures could be examined by photoluminescence (PL), as exaggerated emissions can be observed due to defect densities and oxygen vacancies [86]. Typical PL spectra of ZnO structures show two characteristic emissions due to excitonic states (near-ultraviolet region, 200–400 nm) and structural defects, oxygen vacancies and impurities (visible region, 400–650 nm) [40, 122]. The broad emission band is attributed to deep defects such as oxygen vacancies, V_O (~ 1.62 eV), oxygen interstitials, O_i (~ 2.28 eV), oxygen anti-sites, O_{Zn} (~ 2.38 eV), zinc interstitials, Zn_i (~ 2.90 eV) and zinc vacancies, V_{Zn} (~ 3.06 eV) [38, 40, 127]. On the other hand, it is possible to observe the orange luminescence (OL) and the yellow luminescence (YL) due to the radiative recombination of localized electrons with holes trapped deeply in the oxygen interstitials (O_i) located around 2.14 and 2.2 eV below the conduction band, respectively [122, 128].

The PL spectra under excitation of wavelength 325 nm (~ 3.82 eV), 488 nm (~ 2.54 eV) and 514 nm (~ 2.41 eV) at room temperature are shown in Fig. 7. For the ZnO NPs obtained by method-1, a broad emission peak is observed in the visible region at 606 nm (2.05 eV) and 593 nm (2.09 eV) when excitation light of 325 and 488 nm were used, respectively. In both cases, the emission peaks are due to a Zn_i to O_i transition. When lower energy excitation light (514 nm) is applied, 4 peaks in the range of 525 nm (2.36 eV) to 555 nm (2.24 eV) are clearly observed. These emissions are attributed to the transition between oxygen vacancy (V_O) and interstitial oxygen (O_i) [129, 130]. Likewise, two not very defined absorptions are reported at 623 and 640 nm. These emissions were ascribed to oxygen interstitials [130]. For the sample obtained by method-1, the characteristic emission peak of ZnO NPs located close to 380 nm is not observed.

The PL spectra of ZnO NPs obtained by method-2 as well as the commercial reference sample exhibit an emission in

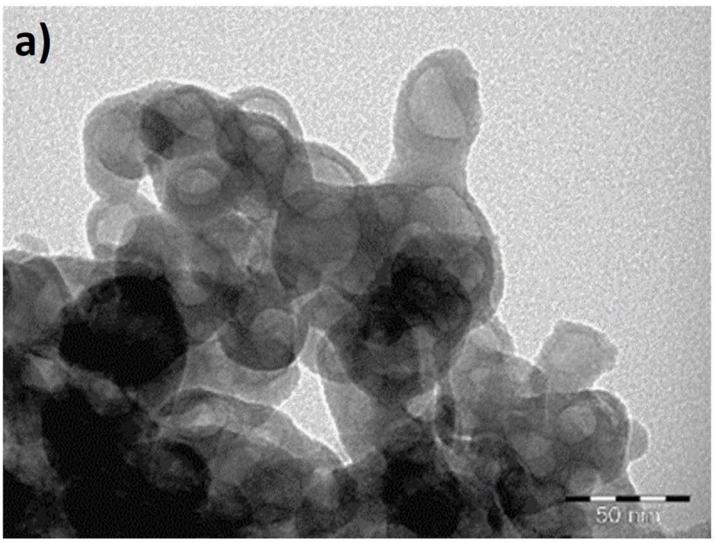
a)
50 nm

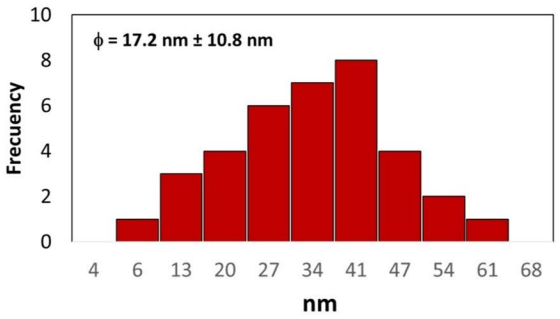
ϕ = 17.2 nm ± 10.8 nm
Frecuency
10
8
6
4
2
0
4 6 13 20 27 34 41 47 54 61 68
nm

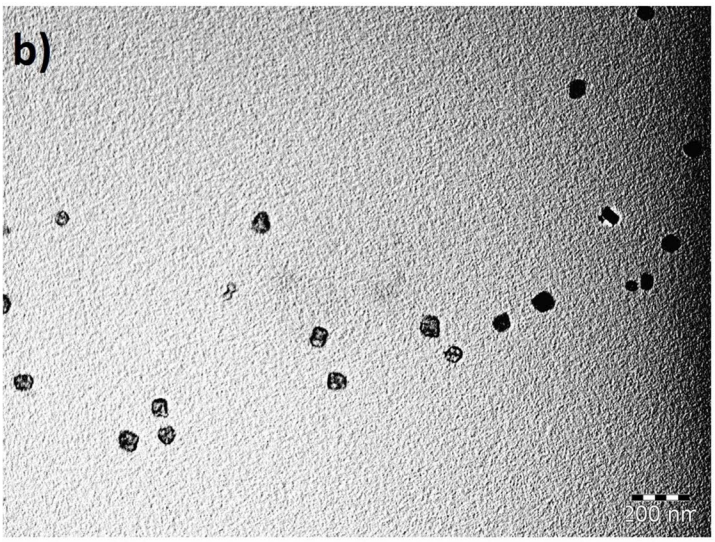
b)
200 nm

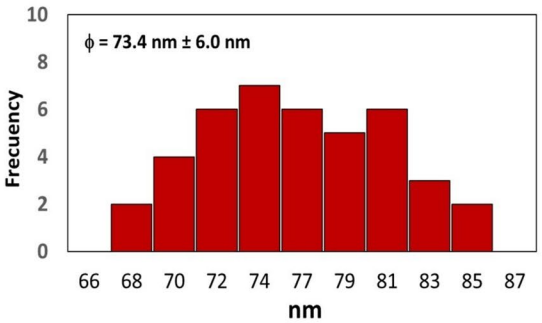
ϕ = 73.4 nm ± 6.0 nm
Frecuency
10
8
6
4
2
0
66 68 70 72 74 77 79 81 83 85 87
nm

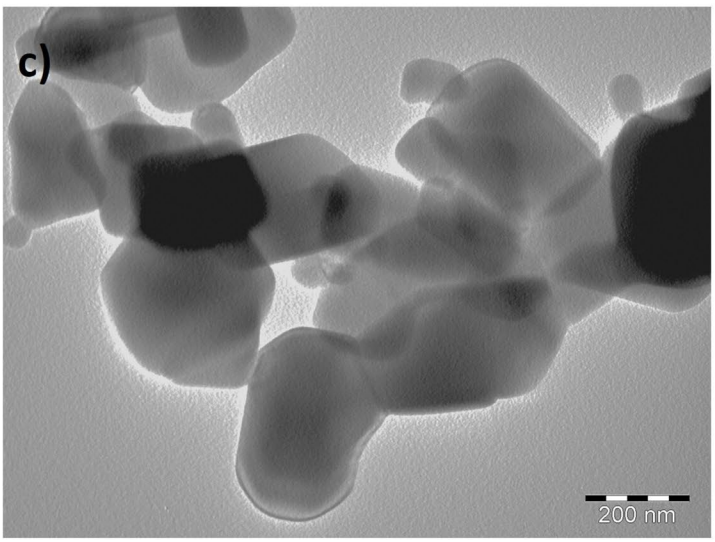
c)
200 nm

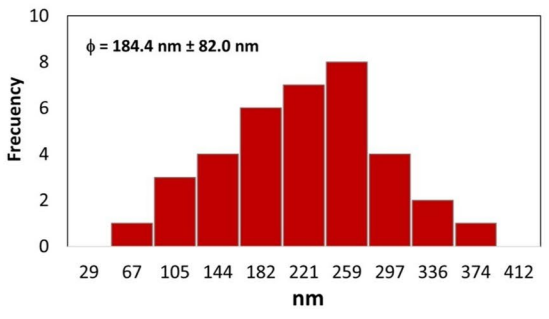
ϕ = 184.4 nm ± 82.0 nm
Frecuency
10
8
6
4
2
0
29 67 105 144 182 221 259 297 336 374 412
nm

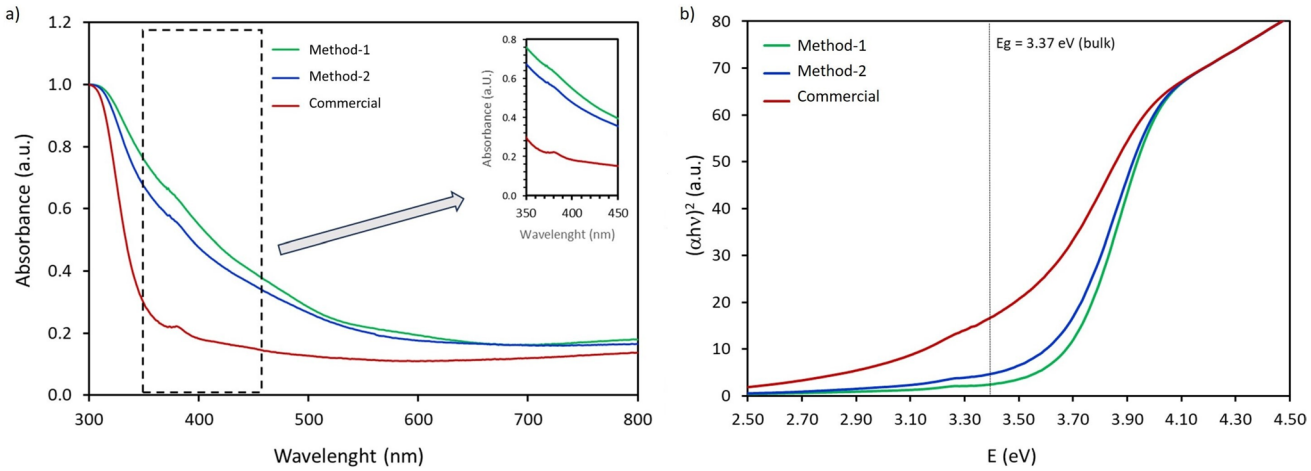

Fig. 6 **a** UV–Vis spectra of synthesized ZnO NPs by chemical precipitation, combustion in solution and commercial sample. The recorded spectra screened in the wavelength range 300–800 nm. **b** Band gap energy of ZnO nanoparticles

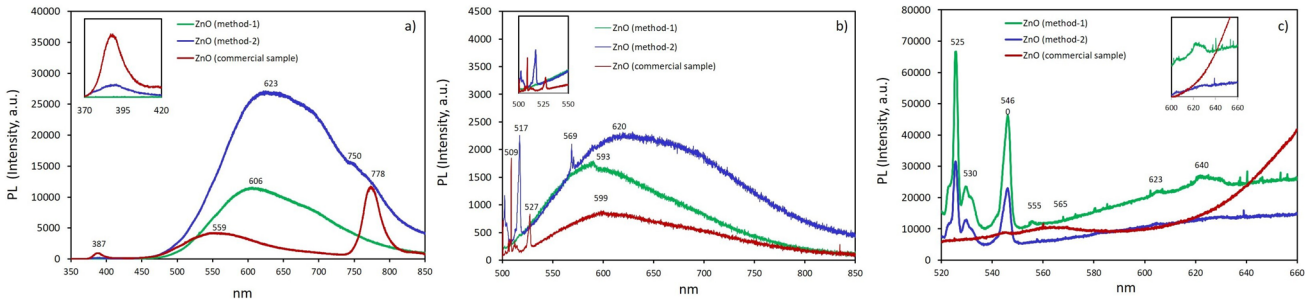

Fig. 7 Room temperature PL spectra of ZnO nanoparticles obtained by chemical precipitation, combustion in solution and commercial sample under excitation of wavelength **a** 325 nm, **b** 488 nm and **c** 514 nm. The recorded spectra screened in the wavelength range 350-880 nm. Spectra were acquired for 10 s with 3 accumulations

the ultraviolet region when the samples are under 325 nm excitation [71]. For the ZnO NPs prepared by method-2, the PL spectra show a sharp peak at 387 nm (3.21 eV) and a broad peak emission at 623 nm (1.99 eV). The first is attributed to near-band-edge (NBE) emission due to radiative recombination of free excitons [40, 90, 124, 129, 131]. While the second is attributed to defects such as oxygen vacancies [38, 128]. Similar to the results shown for the sample obtained by method-1, when a 514 nm excitation source is used, the ZnO Nps prepared by method-2 show 4 defined peaks between the range of 525 and 555 nm. nm, which are attributed to the transition between the Zinc vacancy and interstitial oxygen [47]. While, for the commercial sample, only a small shoulder at 565 nm is observed. Furthermore, in the PL spectrum at 488 nm of the commercial sample, an emission band centered at approximately 778 nm (1.59 eV) in the near-infrared (NIR) region was observed. This unexpected pure NIR peak at 778 does not conform to any energy difference of band-to-band transition and defect levels, therefore, the origin of this NIR peak is considered to be related to the change of Fermi energy level of ZnO [132]. Previous reports have confirmed that surface morphology, presence of impurities, different ratio of Zinc and Oxygen, crystal orientation could influence the work function of ZnO [71]. On the other hand, it is possible to attribute this behavior to the size of the particles in the sample. Wang et al. [105] reported an interesting peak at 759 nm (1.63 eV) in PL spectra for ZnO samples that had been annealed at 1000 °C, demonstrating that it is possible to observe this type of emissions for large particles. For the three samples, no emissions are observed in the blue region.

The crystal size confinement and surface impacts of ZnO Nps not only influence the bandgap but also influence the different optical transitions [132]. This has been evidenced with PL, since different emissions are observed for each sample of ZnO Nps constituted by different average sizes and different synthesis methods [133–137].

On the other hand, many authors indicate that the mechanism of the defects related to the visible luminescence of ZnO remains controversial and needs extensive debate and

Table 4 Emission lengths of the PL spectra of the ZnO Nps samples under excitation of wavelength 325, 488 and 514 nm

Excitation wavelength	UV	Visible emission				Sample
	NBE	Green	Yellow	Orange	Red	
325 nm			606 nm			ZnO (method-1)
488 nm			593 nm			
514 nm		525 nm		623 nm		
		530 nm		640 nm		
		546 nm				
		555 nm				
325 nm	387 nm			623 nm		ZnO (method-2)
488 nm		517 nm		620 nm		
		569 nm				
514 nm		526 nm				
		530 nm				
		546 nm				
		555 nm				
325 nm	387 nm	559 nm			750 nm	ZnO (commercial)
488 nm		509 nm	599 nm			
		527 nm				
514 nm		565 nm				

in-depth analysis [126, 138]. A summary of these results is presented in Table 4.

Application to LFPs Detection

Because LFPs are poorly visible to the naked eye, it is necessary to use a chemical reagent for their development. In the 1970s, LFPs were developed with $AgNO_3$. However, later other chemical inputs such as ninhydrin and iodine were used [23]. On the other hand, in addition to the specific chemical reagent, it is possible to use different development methods depending on the surface where the LFP has been left. The most commonly used methods are summarized in Table 5. Although the powder dusting technique has some drawbacks, it remains the widely used technique because it is simple to apply and requires minimal training. In fact, in the last two decades, research has been carried out with various nanoparticles in order to improve the quality of LFP development (Table 6). The first nanoparticles used were Au, CdSe and ZnO, followed by those of carbon NPs, conjugate polymers, electrodeposition of metal (EDM) NPs, quantum dots, rare earth metal (REM) NPs and SiO_2. However, Au, SiO_2 and ZnO NPs have been found to be the most used nanoparticles for the enhancement of latent fingerprint quality [22].

Following the methodology proposed by Choi et al. [41], LFPs were collected on various non-porous surfaces. The LFPs were recorded on aluminum foil, black glass, clear glass and stainless steel. ZnO Nps applied to the studied surfaces are possibly impregnated by a hydrophobic interaction between them and the sebaceous residues of the LFP [139]. In addition to mechanical adhesion forces, physisorption and chemisorption phenomena contribute individually or simultaneously to the adhesion of ZnO Nps onto LFPs deposited on non-porous surfaces [140]. The palms of the hands have apocrine, eccrine and sebaceous glands that, through secretions, leave LFPs on non-porous surfaces. These residues are composed of water, inorganic and organic compounds (0.5%) [141–144].

The main inorganic components are inorganic salts containing bicarbonate, bromide, calcium, chloride, fluoride, iodide, iron, phosphate, potassium and sodium [6]; while the main organic compounds are some amino acids, lipids (cholesterol, fatty acids, glycerides, long-chain fatty acid esters, squalene, sterols and other lipid esters), proteins and some sugars [6, 145]. Among the most abundant amino acids frequently found in LFPs we can mention alanine, aspartic acid, glycine, histidine, ornithine, serine, threonine and valine [6, 142, 146]. However, over time, small volatile molecules in the LFP residues will be lost through evaporation; while other organic compounds such as long-chain fatty acids, lipids, sterols and inorganic salts will remain present on non-porous surfaces for a longer period of time [140, 147]. Then, the chemical interaction (chemisorption) with the ZnO Nps will be mainly with these substances.

Amino acids have aromatic rings, carboxyl and amino groups that are active sites to interact with external molecules [148]. Previous studies on the interaction between ZnO materials and amino acids have shown that tyrosine has the highest binding energy (7 kJ mol^{-1}), a value comparable to that of hydrogen bonds in a protein (~ 6 kJ mol^{-1}) [149]. This type of interaction is possible since tyrosine and

Table 5 Comparison of conventional methods for latent fingerprint (LFP) development

Method	Procedure	Advantage	Disadvantage
Powder dusting	Powder particles are mechanically or physically adhered to LFPs residues	Simple application and minimal training needed	Possible contamination by DNA transfer from brushes. Low Contrast. The examiner must know which powder to choose
Cyanoacrylate fuming	Polymerization of cyanoacrylate esters monomers on LFP residues that covers the raised fingermark ridges	Effective technique to develop LFP on all nonporous substrates.	Lacks contrast, needing further enhancement with fluorescent dyes. Health and safety issues due to the toxic properties of cyanoacrylate.
Silver nitrate	Reaction of silver nitrate with chloride present in the LFP residues	Simple and effective method	Needs light irradiation or a reducing agent.
Physical developer	Attractive electrostatic forces between charged colloidal silver particles and fingerprint residues, by reaction with lipids and fatty acids present in the LFP residue	Excellent contrast	Surface pretreatment is required, which takes a long time
Ninhydrin	Reaction of ninhydrin with amino acids present in the LFP residues	Simple, effective and has low toxicity.	The development reaction often requires strict control of humidity, light, oxygen, pH and temperature to avoid decreased sensitivity and contrast
DFO (1,8-diazafluoren-9-one)	Reaction of DFO with amino acids present in the LFP residues	The reaction product is fluorescent under green light	The development reaction requires high temperature and low humidity. Health and safety issues due to the toxic and carcinogenic properties of DFO
1,2-Indandione	Reaction of 1,2-indandione with amino acids present in the LFP residues	The reaction product is fluorescent under green light	To produce luminescence is necessary the addition of a zinc metal salt to 1,2-indandione. Is time consuming
Infrared reflection	Process in which infrared light is reflected off the surface containing the LFPs	It works better when one knows where to look for latent fingermarks	Information of other exogenous substances can be obtained (i.e., drugs)
Ultraviolet reflection	Reflected long-wave UV is used to illuminate the substrates where the LFPs are located previously sprayed with developer agent	Applicability on a wide range of substrates	DNA on fingermarks can be damaged Process might be harmful for the user of the method
Fluorescence	Fluorescence images of LFPs on a variety of substrates are obtained by irradiating the sample under light of different wavelengths	Achieves the best visualization compared to other optical techniques	Pretreatment of the sample might be needed
Raman Imaging	Process in which the surface containing the LFPs is subjected to Raman spectroscopic analysis	Pretreatment is necessary for high-quality visualization	Information of other exogenous substances can be obtained (i.e., drugs)
Scanning Electron Microscopy	Surfaces containing LFPs are analyzed by Scanning Electron Microscopy	A high-grade fingermark can be visualized. Morphology and composition of fingermark can be obtained	Usually better after the fingermark has been enhanced with other method
Thermal development	Use heat or steam for the development of white fingerprints on darker backgrounds	Older fingermarks could be visualized	Unreliable results most of the time
Metal-containing nanoparticles/small particle reagents	Metal nanoparticles are applied to LFPs to improve development	Also applicable on older fingermarks	Often extra illumination with UV light is needed

Table 5 (continued)

Method	Procedure	Advantage	Disadvantage
Vacuum metal deposition	Physical process of coating LFPs with very a thin metal film under high vacuum	Can be applied on wetted surfaces	Competent Personnel is needed
Matrix-assisted Laser Desorption Ionization Mass Spectrometry Imaging (MALDI-MSI)	Process in which the surface containing the LFP is analyzed by MALDI-MSI	A high-grade fingermark can be visualized	Fingermark Requires pretreatment

Adapted from Chadwick et al. [10], Christofidis et al. [11] and Gomes et al. [6]

tryptophan interact with ZnO Nps through their aromatic ring, indole group and phenol, respectively [150]. On the other hand, interactions of ZnO nanorods with peptides were favorable according to the negative estimated values of Gibbs free energy change, ΔG (-6 and -8.5 kcal mol^{-1}) and high binding affinity values, K_A ($> 10^4$ M^{-1}) [151]. This confirms that ZnO Nps can adhere by chemisorption to amino acids and peptides of LFPs deposited on non-porous surfaces.

In the case of physisorption, Do et al. [152] found that the nature of the adsorption of phosphate ions on ZnO nanorods was spontaneous ($\Delta G = -8.63$ kJ mol^{-1}), which would corroborate the easy incorporation of ZnO Nps to LFPs on non-porous surfaces. In the process of chemisorption, the electronic structure of the linking molecules or atoms changes, forming covalent or ionic bonds. While in physisorption, no changes occur in the structure of the chemical bonds. This behavior can be explained by the weak van der Waals forces that occur between the adsorbent and adsorbed substances. Whether by one mechanism or another, the ZnO Nps remain adhered to the LFPs deposited on non-porous surfaces. The details of LFPs ridges are generally described in a hierarchical order at three levels: level 1 (pattern), level 2 (minutia points) and level 3 (pores and ridge contours) [153–157, 170].

The LFPs on the surfaces were examined with UV light (360 nm). Afterwards, the LFPs developed on the surfaces were photographed (Fig. 8). The excitation of the nanoparticles with UV light gives rise to the luminescent process [60]. The colors emitted by the three samples of ZnO NPs allowed visualizing the furrows and bifurcations of the LFPs [25, 33, 37, 40, 41, 158]. Acceptable contrast between fingerprints and background is observed on aluminum foil, clear glass and stainless-steel surfaces (Fig. 8). In contrast, LFPs on the black glass surface appear imprecise.

In Fig. 8 it can be seen that all LFPs show a form of whorl fingerprint, which corresponds to one of the three general categories (level 1: global fingerprint pattern) [157]. In addition, it is observed that with all ZnO samples it is possible to identify the pattern core (level 2) of the LFPs on all surfaces. Although, it is less evident on clear glass surface with the commercial ZnO sample (Fig. 8b). The ZnO Nps samples (method-1) and (method-2) show level 2 patterns (core and bifurcation) for all surfaces. Furthermore, the ZnO Nps sample (method-1) allows the identification of other level 2 patterns (island and ending ridge) on the black and clear glass surfaces (Fig. 8b, c). On the other hand, this ZnO Nps sample allows us to observe sweat pores (level 3) on aluminum, clear glass and stainless-steel surfaces (Fig. 8a–c). The results are summarized in Table 7.

Conversely, the best performance of LFP development with ZnO Nps (method-2) is found on black glass and aluminum surfaces with an ending ridge and island pattern

Table 6 Summary of fingerprint detection on various surfaces with the prepared ZnO Nps and compared with other nanoparticles reported in the literature

Nanoparticles	Mean diameter (nm)	Synthesis method	Substrate	References
Ag	10.66 ± 1.22 nm, 12.50 ± 2.64 nm, 14.44 ± 2.68 nm	Chemical reduction	Porous paper	[179]
Au	2.5	Chemical reduction	Glass slide, plastic, tin foil	[174]
Au	3 nm	Sputtering	Clear glass, paper, plastic	[173]
Au	12.5 ± 2.4 nm	Chemical reduction	Non bleached paper, low density polyethylene (LDPE), bags and polypropylene (PP) sheets	[171]
Au–Ag	2–3 nm	Multimetal deposition	Paper	[172]
Au–ZnO	–	Multimetal deposition	Plastic	[59]
BiOCl:Dy^{3+}.Ba^{2+} (co-doped)	–	Solid-state reaction	Plastic lid	[180]
$CaAl_2O_4$:X (X = Tb^{3+}, Ce^{3+}, K^+, Li^+, Na^+)	26–36 nm	Combustion	Plastic sheet, glass marble, stainless steel, ceramic tile, wood	[178]
CdSe/ZnS	3 nm	Multimetal deposition	Paper	[172]
CeO_2	3.1 nm	Co-precipitation	Clear glass	[25]
Fe_2O_3	11.1 nm	Co-precipitation	Clear glass	[25]
Fe_3O_4@SiO_2-CdTe	30 nm	Co-precipitation	Glass slide, black plastic, ceramic, black paper, banknote, period table and leather	[32]
Fe_3O_4, Fe_3O_4@Ag	120–150	Co-precipitation	Paper, plastic, metal, leather	[170]
SiO_2	90.2 + 4.7	Microemulsion	Aluminum, foil, transparent, polypropylene plastic, green polyethylene plastic	[177]
SiO_2 (funcionalized)	72.9 nm	Reverse microemulsion	Aluminum foil, transparent PP film, green PE film	[175, 176]
SiO_2 (funcionalized)	94.6 nm, 95.2 nm	Chemical process	Glass, polystyrene	[30]
TiO_2	4 nm	Sol–gel	Clear glass	[25]
Y_2O_3:Eu^{3+}	80–120 nm	Precipitation	Metal, plastic, and glass	[28]
Y_2O_3:Fe	17–23 nm	Combustion in solution	Leaf, aluminum, marble	[31]
YVO_4:Eu	40	Hydrothermal	Transparent glass	[29]
ZnO	17.2 ± 10.8	Precipitation	Aluminum foil, black glass, stainless steel, clear glass	Current study
ZnO	73.4 ± 6.0	Combustion in solution	Aluminum foil, black glass, stainless steel, clear glass	

(level 2). While on clear glass and stainless steel, level 3 patterns are observed: sweat pores and wrinkles, respectively. The best result obtained for commercial ZnO is observed on the stainless-steel surface. Though, these results only reached patterns of level 2. A comparison of the results obtained with previous studies that have also used ZnO Nps are presented in Table 8. It is observed that previously tested undoped ZnO Nps samples have sizes less than 50 nm, except those reported by Verma et al. [42] and Zargham et al. [44]. It can be seen that the ZnO samples prepared by method-1 and method-2 can reveal LFPs on non-porous surfaces in a similar way to that reported previously, including dark glass.

On the other hand, in addition to being potential LFP developers, the synthesized ZnO nanoparticles could be used in other applications. Among its potential uses we can mention biomedical [46–48, 159–162], antibacterial [45, 85, 86, 85–86, 159–161], anticancer activity through induction of cancer cell apoptosis [46, 159–162], antifungal [87, 160, 161], anti-inflammatory drugs [88, 159–161], antioxidant [45, 84, 88], drug delivery [46, 160, 163], nanobiosensors [164–169] and photocatalytic applications [45, 55, 63, 85,

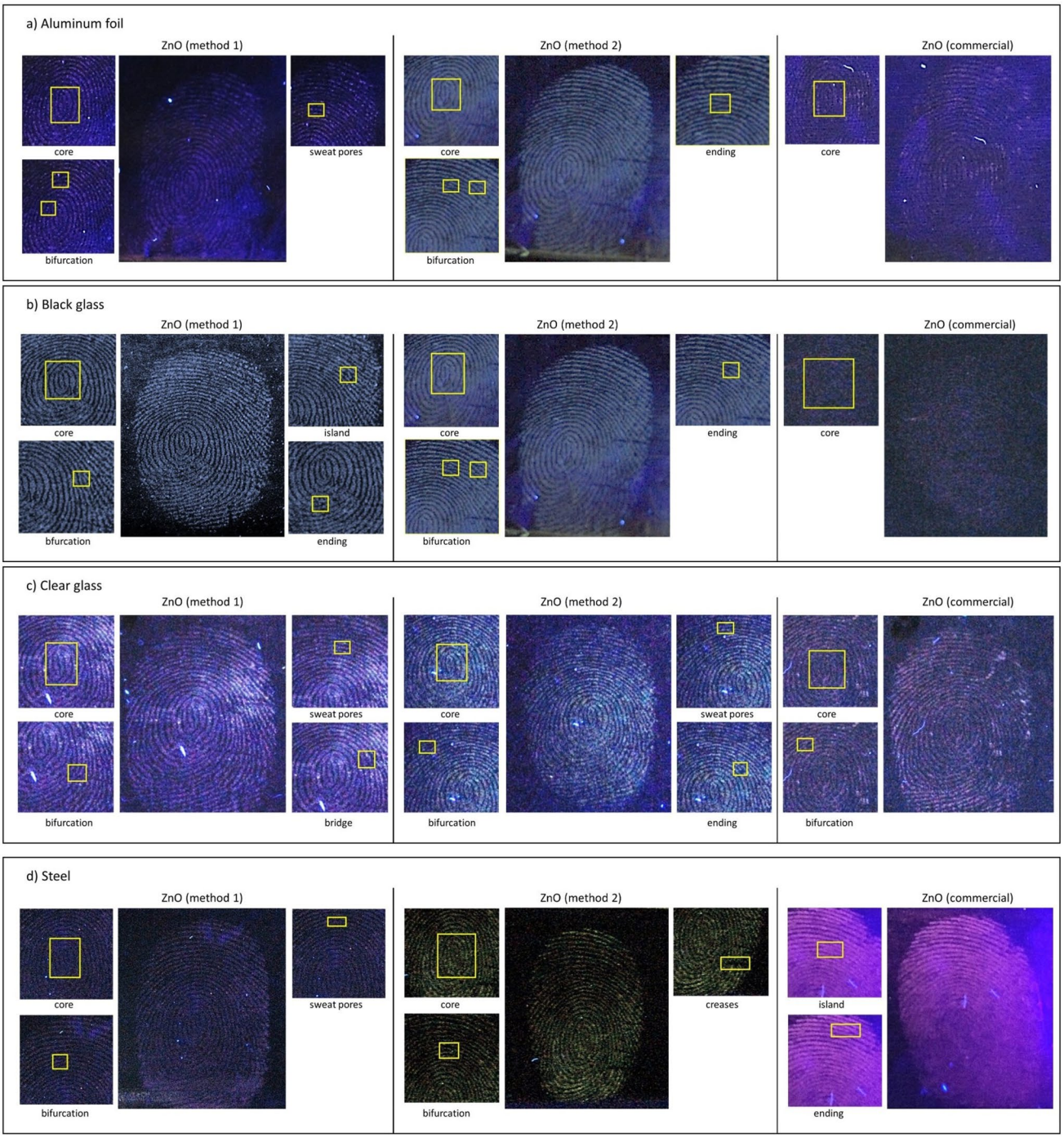

Fig. 8 Reveal of the LFPs impregnated with ZnO nanoparticles obtained by chemical precipitation, combustion in solution and commercial sample on non-porous surface of **a** aluminum foil, **a** black glass, **c** clear glass and **d** stainless steel. Surfaces were illuminated with a 360 nm laser

86, 113]. However, it will be necessary to implement specific tests to determine the effectiveness of the ZnO nanoparticles prepared in each of the previously mentioned applications.

Limitations of this Study

Although it has been proven that the ZnO Nps obtained by chemical precipitation (method-1) and combustion in solution (method-2) can be used as potential LFP developers on non-porous surfaces, we have not been successful in testing

Table 7 Detail of LFP detection levels in the substrates evaluated and compared with those reported in the literature.

Sample	Mean diameter (nm)	Synthesis method	Fingerprint recognition system				Ref.
			Aluminum foil	Black glass	Clear glass	Stainless steel	
ZnO	12	Hydrothermal	Level I Level II	–	Level I Level II	–	[37]
ZnO	27–54	Precipitation	Level I	–	–	–	[40]
ZnO	20, 23 and 45	Green	Level I Level II Level III	–	–	–	[60]
ZnO	25–100	Green	–	–	Level I	–	[44]
ZnO	46	Microemulsion	–	–	Level I	–	[25]
ZnO	5	Combustion in solution	–	–	Level I Level II Level III	–	[39]
ZnO	85–225	Precipitation	–	–	Level I Level II	Level I Level II	[42]
ZnO (method-1)	17.2 ± 10.8	Precipitation	Level I Level II Level III	Level I Level II	Level I Level II Level III	Level I Level II	Current study
ZnO (method-2)	73.4 ± 6.0	combustion in solution	Level I Level II	Level I Level II	Level I Level II Level III	Level I Level II Level III	
ZnO (commercial)	184.4 ± 82.0	–	Level I	Level I	Level I, Level II	Level I	

Table 8 Comparison of size, type of synthesis method and substrates of ZnO Nps evaluated in the present research with previously reported works

Nanoparticles	Mean diameter (nm)	Synthesis method	Substrate	References
ZnO	5–23	Combustion in solution	Clear glass	[39]
ZnO	12	Hydrothermal	Aluminium, clear glass, leaves, glass, metal tools	[37]
ZnO	12.8	Hydrothermal	Aluminum foil, glass slide, magnetic strip of debit card, plastic speaker, touch screen of mobile phone, and touchpad of laptop	[37]
ZnO	13	Precipitation	Cellophane tape	[41]
ZnO	14.75	Precipitation	glass, glossy cardboard, plastic	[33]
ZnO	20, 23 and 45	Green	Aluminium	[60]
ZnO	27–54	Precipitation	Aluminium, transparent tape, aluminum sheets, hard plastic, and floor marble	[40]
ZnO	25–100	Green	Clear glass, tin, wood	[44]
ZnO	85–225	Precipitation	Clear glass, stainless steel, black sheet, chair Handle, copper sheet, keylock, phone screen, wooden piece, ATM card, marble, steel, plastic box, glass slide, wooden table	[42]
ZnO	46	Microemulsion	Clear glass	[25]
ZnO	17.2 ± 10.8	Precipitation	Aluminum foil, black glass, stainless steel, clear glass	Current Study
ZnO	73.4 ± 6.0	Combustion in solution	Aluminum foil, black glass, stainless steel, clear glass	
$ZnGa_2O_4$:Mn	7–44	Microwave	Glass, glossy card, paper	[171]
ZnO:La	13–20	Combustion in solution	Wood, mobile, bottle, pocket whorl	[181]
ZnO:N	40–50	Precipitation	Aluminum (foil, rod, sheet), compact disc, magazine paper, iron disc	[172]
ZnO-SiO_2	32.9	Heating	Calculator, cardboard, glass, glazed wrapper, laptop, metallic can, plastic	[173]

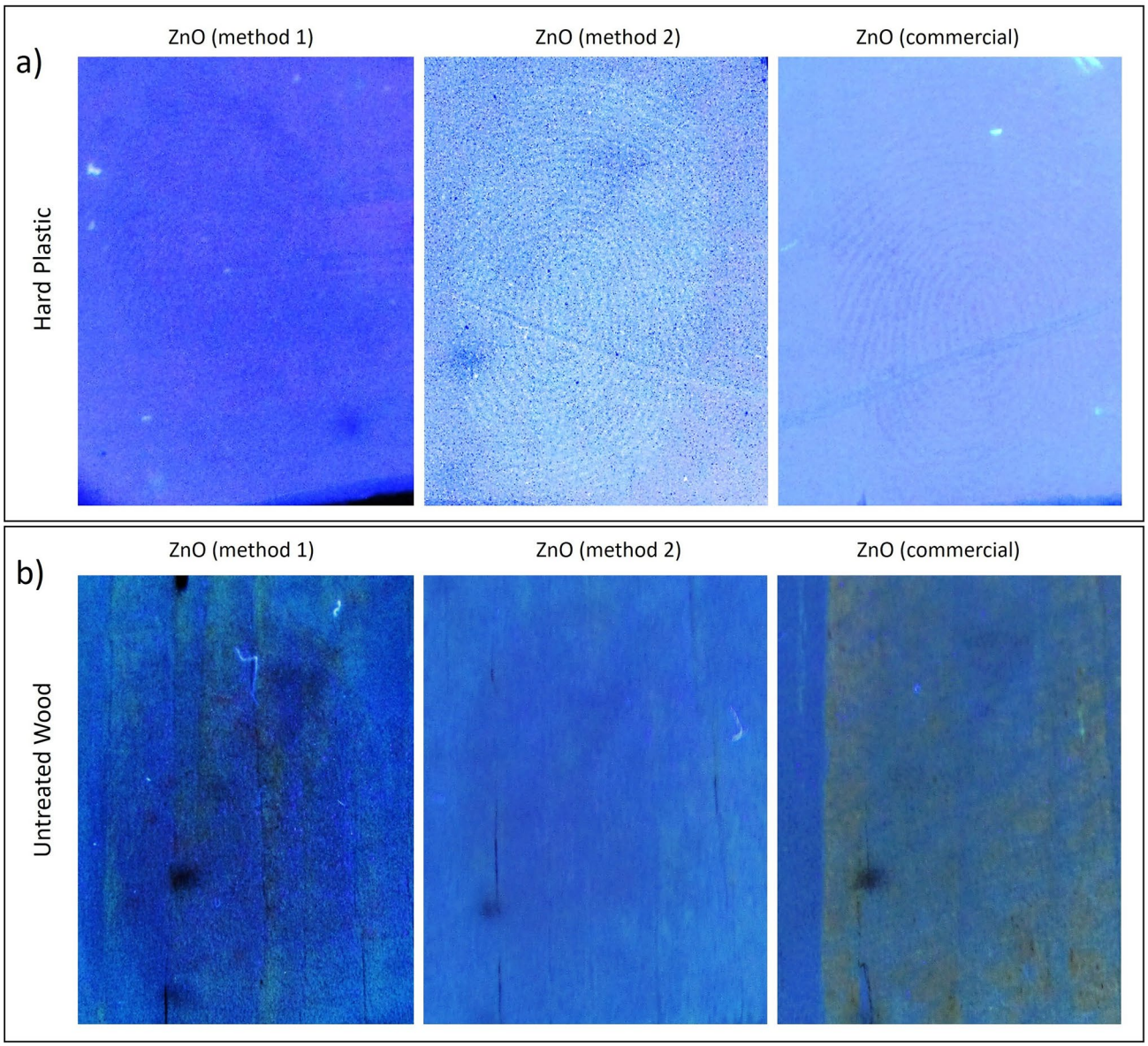

Fig. 9 Reveal of the LFPs impregnated with ZnO nanoparticles obtained by chemical precipitation, combustion in solution and commercial sample on porous surface of **a** plastic and **b** wood. Surfaces were illuminated with a 360 nm laser

them on porous surfaces such as untreated wood and plastic (Fig. 9). Figure 9 shows unclearly the fingerprints deposited on porous surfaces. On hard plastic surface it is only possible to observe in a general way (level I) the fingerprint with the ZnO Nps (method-2). While only a slight stain is observed on the untreated wood with the ZnO Nps (method-1). Unfortunately, the possibility of losing organic substances that compose the LFPs deposited on porous surfaces is high. In fact, few studies on plastic surfaces using ZnO Nps as fingerprint revealers have been reported successfully [37, 40, 42, 43].

Conclusion

In this work, ZnO Nps have been prepared by using chemical precipitation (method-1) and combustion in solution (method-2). Both synthesis methods allow obtaining hexagonal wurtzite-type ZnO crystal structures with mean diameters of 17.2 nm ± 10.8 nm (method-1) and 73.4 nm ± 6.0 nm (method-2). Semispherical and semi-square ZnO NPs where obtained when the method-1 and method-2 were applied. The band gap value of ZnO Nps obtained by method-1 (3688 eV) and method-2 (3591 eV) were higher than that of the bulk material (3.37 eV) which verifies the confinement effect due to the decrease in particle size. PL indicated the

presence of crystalline defects since emissions are observed in the visible range. It is possible to observe the LFPs on the non-porous surfaces studied, since level 2 and level 3 patterns of the fingerprint recognition system can be visualized. The ZnO Nps obtained can be used to reveal LFPs on aluminum, stainless steel, clear and black glass surfaces. However, it is necessary to improve the photo taking technique.

Supplementary Information The online version contains supplementary material available at https://doi.org/10.1007/s10876-025-02770-w.

Acknowledgments The authors acknowledge the Center of Materials Analysis of the PUCP (CAM-PUCP) for the facilities to carry out the Raman and XRD analyses.

Author Contributions MG: Conceived the idea and designed the experiments, Supervision, Writing—original draft, Writing—review & editing. BF: Performed the experiments and data analysis. RG: Contributes with XRD analysis, Formal analysis. AQ: Contributes with Raman analysis, Formal analysis. LM: Contributes with TEM analysis. SG: contributes contributed with resources.

Funding Open access funding provided by Pontificia Universidad Catolica del Peru. Not applicable.

Data Availability Data is provided within the manuscript or supplementary information files

Declarations

Conflict of interest The authors declare that they have no known competing financial interests or personal relationships that could have appeared to influence the work reported in this paper.

Ethical Approval Not applicable.

References

1. S. A. Cole and M. Lynch, Chapter 6—DNA profiling versus fingerprint evidence: More of the same?, in R. Hindmarsh and B. Prainsack (eds.), *Genetic Suspects: Global Governance of Forensic DNA Profiling and Databasing* (Cambridge University Press, London, 2010), pp. 105–128. https://doi.org/10.1017/CBO9780511778193.007.
2. M. Carlin, R. Nickel, K. Halstead, J. Viray, A. Hall, and A. Ehrlich (2023). Quantifying DNA loss in laboratory-created latent prints due to fingerprint processing. *Forensic Sci. Int.* **344**, 1–7. https://doi.org/10.1016/j.forsciint.2023.111595.
3. A. S. Bathrick, S. Norsworthy, D. T. Plaza, M. N. McCormick, D. Slack, and R. S. Ramotowski (2022). DNA recovery after sequential processing of latent fingerprints on copy paper. *J. Forensic Sci.* **67**, 149–160. https://doi.org/10.1111/1556-4029.14881.
4. R. Dhaneshwar, M. Kaur, and M. Kaur (2021). An investigation of latent fingerprinting techniques. *Egypt. J. Forensic Sci.* **11**, 1–15. https://doi.org/10.1186/s41935-021-00252-4.
5. J. B. Friesen (2015). Forensic chemistry: The revelation of latent fingerprints. *J. Chem. Educ.* **92**, 497–504. https://doi.org/10.1021/ed400597u.
6. F. M. Gomes, C. M. Pereira de Pereira, K. C. Mariotti, T. M. Pereira, N. Araujo dos Santos, and W. Romão (2023). Study of latent fingerprints—A review. *Forensic Chem.* **35**, 1–13. https://doi.org/10.1016/j.forc.2023.100525.
7. A. Khuu, X. Spindler, and C. Roux (2020). Detection of latent fingermarks and cells on paper. *Forensic Sci. Int.* **309**, 1–7. https://doi.org/10.1016/j.forsciint.2020.110185.
8. C. G. Worley, S. S. Wiltshire, T. C. Miller, G. J. Havrilla, and V. Majidi (2006). Detection of visible and latent fingerprints using micro-X-ray fluorescence elemental imaging. *J. Forensic Sci.* **51**, 57–63. https://doi.org/10.1111/j.1556-4029.2005.00006.x.
9. G. S. Bumbrah (2016). Small particle reagent (SPR) method for detection of latent fingermarks: A review. *Egypt. J. Forensic Sci.* **6**, 328–332. https://doi.org/10.1016/j.ejfs.2016.09.001.
10. S. Chadwick, S. Moret, N. Jayashanka, C. Lennard, X. Spindler, and C. Roux (2018). Investigation of some of the factors influencing fingermark detection. *Forensic Sci. Int.* **289**, 381–389. https://doi.org/10.1016/j.forsciint.2018.06.014.
11. G. Christofidis, J. Morrissey, and J. W. Birkett (2018). Detection of fingermarks-applicability to metallic surfaces: A literature review. *J. Forensic Sci.* **63**, 1616–1627. https://doi.org/10.1111/1556-4029.13775.
12. R. M. Connatser, S. M. Prokes, O. J. Glembocki, R. L. Schuler, C. W. Gardner, S. A. Lewis, and L. A. Lewis (2010). Toward surface-enhanced raman imaging of latent fingerprints. *J. Forensic Sci.* **55**, 1462–1470. https://doi.org/10.1111/j.1556-4029.2010.01484.x.
13. A. A. Frick, P. Fritz, and S. W. Lewis, Chapter 9—Chemical methods for the detection of latent fingermarks, in J. A. Siegel (ed.), *Forensic Chemistry: Fundamentals and Applications* (John Wiley & Sons, New York, 2016), pp. 354–399. https://doi.org/10.1002/9781118897768.
14. G. S. Sodhi and J. Kaur (2001). Power method for detecting latent fingerprints: A review. *Forensic Sci. Int.* **120**, 172–176. https://doi.org/10.1016/S0379-0738(00)00465-5.
15. G. S. Sodhi and J. Kaur (2016). Physical developer method for detection of latent fingerprints: A review. *Egypt. J. Forensic Sci.* **6**, 44–47. https://doi.org/10.1016/j.ejfs.2015.05.001.
16. M. Tahtouh, J. R. Kalman, C. Roux, C. Lennard, and B. J. Reedy (2005). The detection and enhancement of latent fingermarks using infrared chemical imaging. *J. Forensic Sci.* **50**, 64–72. https://doi.org/10.1520/JFS2004213.
17. S. P. Wargacki, L. A. Lewis, and M. D. Dadmun (2007). Understanding the chemistry of the development of latent fingerprints by superglue fuming. *J. Forensic Sci.* **52**, 1057–1062. https://doi.org/10.1111/j.1556-4029.2007.00527.x.
18. C. Yuan, M. Li, M. Wang, H. Cao, and T. Lin (2021). A critical review of fundamentals and applications of electrochemical development and imaging of latent fingerprints. *Electrochim. Acta* **390**, 1–5. https://doi.org/10.1016/j.electacta.2021.138798.

19. E. Prabakaran and K. Pillay (2020). ZnONPs nanocomposite for latent fingerprint detection by using powder brushing method. *Arab. J. Chem.* **13**, 3817–3835. https://doi.org/10.1016/j.arabjc.2019.01.004.
20. E. Prabakaran and K. Pillay (2021). Nanomaterials for latent fingerprint detection: A review. *J. Mater. Res. Technol.* **12**, 1856–1885. https://doi.org/10.1016/j.jmrt.2021.03.110.
21. M. Wang, M. Li, A. Yu, Y. Zhu, M. Yang, and C. Mao (2017). Fluorescent nanomaterials for the development of latent fingerprints in forensic sciences. *Adv. Funct. Mater.* **27**, 1–16. https://doi.org/10.1002/adfm.201606243.
22. V. Prasad, S. Lukose, P. Agarwal, and L. Prasad (2020). Role of nanomaterials for forensic investigation and latent fingerprinting—a review. *J. Forensic. Sci.* **65**, 26–36. https://doi.org/10.1111/1556-4029.14172.
23. V. Sharma, S. Choudhary, P. Mankotia, A. Kumari, K. Sharma, R. Sehgal, and V. Kumar (2021). Nanoparticles as fingermark sensors. *Trend. Anal. Chem.* **143**, 1–29. https://doi.org/10.1016/j.trac.2021.116378.
24. D. S. Bhagat, I. V. Suryawanshi, W. B. Gurnule, S. S. Sawant, and P. B. Chavan (2021). Greener synthesis of CuO nanoparticles for enhanced development of latent fingerprints. *Mater. Today Proc.* **36**, 747–750. https://doi.org/10.1016/j.matpr.2020.05.357.
25. M. O. Amin, M. Madkour, and E. Al-Hetlani (2018). Metal oxide nanoparticles for latent fingerprint visualization and analysis of small drug molecules using surface-assisted laser desorption/ionization mass spectrometry. *Anal. Bioanal. Chem.* **410**, 4815–4827. https://doi.org/10.1007/s00216-018-1119-2.
26. P. Kumar, N. Thakur, K. Kumar, S. Kumar, A. Dutt, V. K. Thakur, C. Gutiérrez-Rodelo, P. Thakur, A. Navarrete, and N. Thakur (2024). Catalyzing innovation: Exploring iron oxide nanoparticles—Origins, advancements, and future application horizons. *Coord. Chem. Rev.* **507**, 215750. https://doi.org/10.1016/j.ccr.2024.215750.
27. P. Kumar, S. Kumar, and N. Thakur (2023). Azadirachta indica and polyvinylpyrrolidone encapsulated Fe_2O_3 nanoparticles to enhance the photocatalytic and antioxidant activity. *Inorg. Chem. Commun.* **155**, 111084. https://doi.org/10.1016/j.inoche.2023.111084.
28. A. Askerbay, A. Molkenova, and T. S. Atabaev (2020). Latent fingerprint detection with luminescent Y_2O_3:Eu^{3+} nanoparticles. *Mater. Today Proc.* **20**, 245–248. https://doi.org/10.1016/j.matpr.2019.10.042.
29. M. Wang, M. Li, A. Yu, J. Wu, and C. Mao (2015). Rare earth fluorescent nanomaterials for enhanced development of latent fingerprints. *ACS Appl. Mater. Interfaces.* **7**, 28110–28115. https://doi.org/10.1021/acsami.5b09320.
30. Y. J. Kim, H. S. Jung, J. Lim, S. J. Ryu, and J. K. Lee (2016). Rapid imaging of latent fingerprints using biocompatible fluorescent silica nanoparticles. *Langmuir* **32**, 8077–8083. https://doi.org/10.1021/acs.langmuir.6b01977.
31. P. L. T. Lee, F. K. Kanodarwala, C. Lennard, X. Spindler, V. Spikmans, C. Roux, and S. Moret (2022). Latent fingermark detection using functionalised silicon oxide nanoparticles: Investigation into novel application procedures. *Forensic Sci. Int.* **335**, 111275. https://doi.org/10.1016/j.forsciint.2022.111275.
32. P. L. T. Lee, F. K. Kanodarwala, C. Lennard, X. Spindler, V. Spikmans, C. Roux, and S. Moret (2020). Latent fingermark detection using functionalised silicon oxide nanoparticles: Optimisation and comparison with cyanoacrylate fuming. *Forensic Sci. Int.* **315**, 110442. https://doi.org/10.1016/j.forsciint.2020.110442.
33. D. Luthra and S. Kumar (2018). The development of latent fingerprints by zinc oxide and tin oxide nanoparticles prepared by precipitation technique. *AIP Conf. Proc.* **1953**, 1–4. https://doi.org/10.1063/1.5032584.
34. H. Zhou, H. Chen, R. Ma, X. Lic, X. Du, and M. Zhang (2023). Use of conductive Ti_2O_3 nanoparticles for optical and electrochemical imaging of latent fingerprints on various substrates. *J. Electroanal. Chem.* **936**, 117387. https://doi.org/10.1016/j.jelechem.2023.117387.
35. N. Thakur, N. Thakur, A. Kumar, V. K. Thakur, S. Kalia, V. Arya, A. Kumar, S. Kumar, and G. Z. Kyzas (2024). A critical review on the recent trends of photocatalytic, antibacterial, antioxidant and nanohybrid applications of anatase and rutile TiO_2 nanoparticles. *Sci. Total Environ.* **914**, 169815. https://doi.org/10.1016/j.scitotenv.2023.169815.
36. N. Thakur, N. Thakur, V. Bhullar, S. Sharma, A. Mahajan, K. Kumar, D. P. Sharma, and D. Pathak (2021). TiO_2 nanofibers fabricated by electrospinning technique and degradation of MO dye under UV light. *Z Krist. – Cryst. Mater.* **236**, 239–250. https://doi.org/10.1515/zkri-2021-2025.
37. G. S. Bumbrah, M. Jani, D. S. Bhagat, K. Dalal, A. Kaushal, K. Sadhana, G. Sriramulu, and A. Das (2022). Zinc oxide nanoparticles for detection of latent fingermarks on nonporous surfaces. *Mater. Chem. Phys.* **278**, 1–9. https://doi.org/10.1016/j.matchemphys.2021.125660.
38. M. J. Choi, K. E. McBean, P. H. R. Ng, A. M. McDonagh, P. J. Maynard, C. Lennard, and C. Roux (2008). An evaluation of nanostructured zinc oxide as a fluorescent powder for fingerprint detection. *J. Mater. Sci.* **43**, 732–737. https://doi.org/10.1007/s10853-007-2178-5.
39. N. H. Deepthi, R. B. Basavaraj, S. C. Sharma, J. Revathi, S. Ramani, S. Sreenivasa, and H. Nagabhushana (2018). Rapid visualization of fingerprints on various surfaces using ZnO superstructures prepared via simple combustion route. *J. Sci. Adv. Mater. Devices.* **3**, 18–28. https://doi.org/10.1016/j.jsamd.2018.01.007.
40. S. Pramanik, S. Mukherjee, S. Dey, S. Mukherjee, S. Das, T. Ghosh, P. Ghosh, R. Nath, and P. K. Kuiri (2022). Cooperative effects of zinc interstitials and oxygen vacancies on violet-blue photoluminescence of ZnO nanoparticles: UV radiation induced enhanced latent fingerprint detection. *J. Lumin.* **251**, 1–13. https://doi.org/10.1016/j.jlumin.2022.119156.
41. S. Rajan, A. Venugopal, H. Kozhikkalathil, S. Valappil, M. Kale, M. Mann, P. Ahuja, and S. Munjal (2023). Synthesis of ZnO nanoparticles by precipitation method: Characterizations and applications in decipherment of latent fingerprints. *Mater. Today: Proc.* **1**, 1–4. https://doi.org/10.1016/j.matpr.2023.05.680.
42. R. K. Verma, V. Nagar, V. Aseri, B. Mavry, P. P. Pandit, R. L. Chopade, A. Singh, A. Singh, V. K. Yadav, K. Pandey, and M. S. Sankhla (2022). Zinc oxide (ZnO) nanoparticles: Synthesis properties and their forensic applications in latent fingerprints development. *Mater. Today Proc.* **69**, 36–41. https://doi.org/10.1016/j.matpr.2022.08.074.
43. I. H. Yu, S. Jou, C. M. Chen, K. C. Wang, L. J. Pang, and J. S. Liao (2011). Development of latent fingerprint by ZnO deposition. *Forensic Sci. Int.* **207**, 14–18. https://doi.org/10.1016/j.forsciint.2010.07.035.
44. M. Zargham, M. F. Khan, R. A. Rehman, A. Rakha, R. Nazir, M. Salman, S. Akhtar, S. Nazir, I. Zareef, and A. Munawar (2004). Role of doped ZnO variants for the development of latent fingerprint. *Inorg. Chem. Commun.* **162**, 112269. https://doi.org/10.1016/j.inoche.2024.112269.
45. A. Rana, P. Kumar, N. Thakur, S. Kumar, K. Kumar, and N. Thakur (2024). Investigation of photocatalytic, antibacterial and antioxidant properties of environmentally green synthesized zinc oxide and yttrium doped zinc oxide nanoparticles. *Nano-Struct. Nano-Objects.* **38**, 101188. https://doi.org/10.1016/j.nanoso.2024.101188.

46. J. Jiang, J. Pi, and J. Cai (2018). The advancing of zinc oxide nanoparticles for biomedical applications. *Bioinorg. Chem. Appl.* **2018**, 1–18. https://doi.org/10.1155/2018/1062562.
47. A. M. Al-Mohaimeed, W. A. Al-Onazi, and M. F. El-Tohamy (2022). Multifunctional eco-friendly synthesis of zno nanoparticles in biomedical applications. *Molecules* **27**, 579. https://doi.org/10.3390/molecules27020579.
48. F. Islam, S. Shohag, M. J. Uddin, M. R. Islam, M. H. Nafady, A. Akter, S. Mitra, A. Roy, T. B. Emran, and S. Cavalu (2022). Exploring the journey of zinc oxide nanoparticles (ZnO-NPs) toward biomedical applications. *Materials* **15**, 2160. https://doi.org/10.3390/ma15062160.
49. S. G. Menon, A. K. Kunti, D. E. Motaung, and H. C. Swart (2019). A new recipe for the rapid microwave synthesis of high quantum yield Mn2+-doped $ZnGa_2O_4$ phosphors for potential forensic applications. *New J. Chem.* **43**, 17446–17456. https://doi.org/10.1016/j.arabjc.2019.01.004.
50. H. N. Shivananjaiah, K. S. Kumari, and M. S. Geetha (2020). Green mediated synthesis of lanthanum doped zinc oxide: Study of its structural, optical and latent fingerprint application. *J. Rare Earths* **38**, 1281–1287. https://doi.org/10.1016/j.jre.2020.07.012.
51. N. Thakur and N. Thakur (2024). Degradation of textiles dyes and scavenging activity of spherical shape obtained anatase phase of Co–Ni-doped TiO_2 nanocatalyst. *J. Mater. Sci.: Mater. Electron.* **35**, 134. https://doi.org/10.1007/s10854-023-11851-3.
52. P. Kumar, D. Pathak, and N. Thakur (2024). Trimetallic doped hematite (α-Fe_2O_3) nanoparticles using biomolecules of Azadirachta indica leaf extract for photocatalytic dye removal: Insights into catalyst stability and reusability. *Emergent Mater.* 1–17. https://doi.org/10.1007/s42247-024-00742-w
53. S. Thakur, P. Kumar, N. Thakur, K. Kumar, K. Jeet, S. Kumar, and N. Thakur (2024). Photocatalytic, antibacterial and antioxidant potential of spheroidal shape chromium and yttrium doped cobalt oxide nanoparticles: A green approach. *J. Indian Chem. Soc.* **110**, 101199. https://doi.org/10.1016/j.jics.2024.101199.
54. A. Dakhlaoui, M. Jendoubi, L. S. Smiri, A. Kanaev, and N. Jouini (2009). Synthesis, characterization and optical properties of ZnO nanoparticles with controlled size and morphology. *J. Cryst. Growth* **311**, 3989–3996. https://doi.org/10.1016/j.jcrysgro.2009.06.028.
55. K. J. Rao, V. Kumaravel, I. Pownraj, K. Saha, T. Korumilli, and S. K. Sadasivam (2022). Biosynthesis and photocatalytic evaluation of ZnO nanoparticles using banana flower perianth. *J. Clean. Prod.* **380**, 1–14. https://doi.org/10.1016/j.jclepro.2022.135180.
56. A. Singh, H. P. Gogoi, and P. Barman (2023). Synthesis of metal oxide nanoparticles by facile thermal decomposition of new Co(II), Ni(II), and Zn(II) Schiff base complexes-optical properties and photocatalytic degradation of methylene blue dye. *Inorganica Chim. Acta* **546**, 1–9. https://doi.org/10.1016/j.ica.2022.121292.
57. J. H. Jun, H. Seong, K. Cho, B. M. Moon, and S. Kim (2009). Ultraviolet photodetectors based on ZnO nanoparticles. *Ceram. Int.* **35**, 2797–2801. https://doi.org/10.1016/j.ceramint.2009.03.032.
58. A. Agrawal, R. Sharma, A. Sharma, K. K. Awasthi, K. Awasthi, and A. Awasthi, Chapter 7: ZnO nanostructures for latent fingerprints, in K. K. Awasthi, M. S. Sankhla, S. Lukose, and K. Parihar (eds.), *Friction Ridge Analysis. Materials Horizons: From Nature to Nanomaterials* (Springer, Singapore, 2023), pp. 113–128. https://doi.org/10.1007/978-981-99-4028-8_7.
59. A. Becue, A. Scoundrianos, C. Champod, and P. Margot (2008). Fingermark detection based on the in-situ growth of luminescent nanoparticles—Towards a new generation of multimetal deposition. *Forensic Sci. Int.* **179**, 39–43. https://doi.org/10.1016/j.forsciint.2008.04.008.
60. M. R. Chandana, D. R. Lavanya, B. R. E. Krushna, B. D. Prasad, J. Malleschappa, S. C. Sharma, F. D. Joy, P. Soundararajan, and H. Nagabhushana (2023). Effect of precursors on ZnO nanoparticles to enhance the level-III ridge details of LFPs and anti-counterfeiting applications. *Mater. Sci. Semicond. Process.* **167**, 1–14. https://doi.org/10.1016/j.mssp.2023.107749.
61. M. T. Noman, N. Amor, and M. Petru (2022). Synthesis and applications of ZnO nanostructures (ZONSs): A review. *Crit. Rev. Solid State Mater. Sci.* **47**, 99–141. https://doi.org/10.1080/10408436.2021.1886041.
62. S. Flores and O. Chumpitaz (2019). Efecto del cobalto sobre nano-partículas de óxido de zinc en el desempeño anticorrosivo de un imprimante alquídico. *Rev. de Metal.* **55**, 1–10. https://doi.org/10.3989/revmetalm.139.
63. G. Nagaraju, G. C. Shivaraju, G. Banuprakash, and D. Rangappa (2017). Photocatalytic activity of ZnO nanoparticles: Synthesis via solution combustion method. *Mater. Today: Proc.* **4**, 11700–11705. https://doi.org/10.1016/j.matpr.2017.09.085.
64. A. Umar, R. Kumar, G. Kumar, H. Algarni, and S. H. Kim (2015). Effect of annealing temperature on the properties and photocatalytic efficiencies of ZnO nanoparticles. *J. Alloys Compd.* **648**, 46–52. https://doi.org/10.1016/j.jallcom.2015.04.236.
65. M. K. Debanath and S. Karmakar (2013). Study of blueshift of optical band gap in zinc oxide (ZnO) nanoparticles prepared by low-temperature wet chemical method. *Mater. Lett.* **111**, 116–119. https://doi.org/10.1016/j.matlet.2013.08.069.
66. L. K. Jangir, Y. Kumari, A. Kumar, K. Manoj, and K. Awasthi (2017). Investigation of luminescence and structural properties of ZnO nanoparticles, synthesized with different precursors. *Mater. Chem. Front.* **1**, 1413–1421. https://doi.org/10.1039/C7QM00058H.
67. P. K. Samanta, A. Saha, and T. Kamilya (2015). Morphological and optical property of spherical ZnO nanoparticles. *Optik* **126**, 1740–1743. https://doi.org/10.1016/j.ijleo.2015.04.025.
68. A. Becheri, M. Dürr, P. Lo Nostro, and P. Baglioni (2008). Synthesis and characterization of zinc oxide nanoparticles: Application to textiles as UV-absorbers. *J. Nanopart. Res.* **10**, 679–689. https://doi.org/10.1007/s11051-007-9318-3.
69. M. Guzman, B. M. Flores, L. Malet, and S. Godet (2018). Synthesis and characterization of zinc nanoparticles for application in the detection of fingerprint. *Mater. Sci. Forum* **916**, 232–236. https://doi.org/10.4028/www.scientific.net/MSF.916.232.
70. S. Kumar, A. Thakur, V. S. Rangra, and S. Sharma (2016). Synthesis and use of low-band-gap ZnO nanoparticles for water treatment. *Arab. J. Sci. Eng.* **41**, 2393–2398. https://doi.org/10.1007/s13369-015-1852-1.
71. M. J. Chithra, M. Sathya, and K. Pushpanathan (2015). Effect of pH on crystal size and photoluminescence property of ZnO nanoparticles prepared by chemical precipitation method. *Acta Metall. Sin. (Engl. Lett.)* **28**, 394–404. https://doi.org/10.1007/s40195-015-0218-8.
72. T. K. Pathak and H. C. Swart, Chapter 2—Structural and luminescence properties of ZnO Nanoparticles synthesized by mixture of fuel approach in solution combustion method, in A. M. Nahhas (ed.), *Zinc Oxide Based Nano Materials and Devices* (IntechOpen, London, 2019), p. 10. https://doi.org/10.5772/intechopen.78819.
73. A. Varma, A. S. Mukasyan, A. S. Rogachev, and K. V. Manukyan (2016). Solution combustion synthesis of nanoscale materials. *Chem. Rev.* **116**, 14493–14586. https://doi.org/10.1021/acs.chemrev.6b00279.
74. M. J. Choi, A. M. McDonagh, P. Maynard, and C. Roux (2008). Metal-containing nanoparticles and nano-structured particles in

fingermark detection. *Forensic Sci. Int.* **179**, 87–97. https://doi.org/10.1016/j.forsciint.2008.04.027.
75. M. R. Parra and F. Z. Haque (2014). Aqueous chemical route synthesis and the effect of calcination temperature on the structural and optical properties of ZnO nanoparticle. *J. Mater Res Technol.* **3**, 363–369. https://doi.org/10.1016/j.jmrt.2014.07.001.
76. M. M. Ba-Abbad, A. A. H. Kadhum, A. B. Mohamad, M. S. Takriff, and K. Sopian (2013). The effect of process parameters on the size of ZnO nanoparticles synthesized via the sol–gel technique. *J. Alloys Compd.* **550**, 63–70. https://doi.org/10.1016/j.jallcom.2012.09.076.
77. K. G. Akpomie, S. Ghosh, M. Gryzenhout, and J. Conradie (2021). One-pot synthesis of zinc oxide nanoparticles via chemical precipitation for bromophenol blue adsorption and the antifungal activity against filamentous fungi. *Sci. Rep.* **11**, 8305. https://doi.org/10.1038/s41598-021-87819-2.
78. D. Rajesh, B. V. Lakshmi, and C. S. Sunandana (2012). Two-step synthesis and characterization of ZnO nanoparticles. *Phys. B. Condens. Matter* **407**, 4537–4539. https://doi.org/10.1016/j.physb.2012.07.050.
79. M. Kahouli, A. Barhoumi, A. Bouzid, A. Al-Hajry, and S. Guermazi (2015). Structural and optical properties of ZnO nanoparticles prepared by direct precipitation method. *Superlattices Microstruct.* **85**, 7–23. https://doi.org/10.1016/j.spmi.2015.05.007.
80. M. M. Khan, N. H. Saadah, M. E. Khan, M. H. Harunsani, A. L. Tan, and M. H. Cho (2018). Potentials of Costus woodsonii leaf extract in producing narrow band gap ZnO nanoparticles. *Mater. Sci. Semicond. Process.* **91**, 194–200. https://doi.org/10.1016/j.mssp.2018.11.030.
81. M. Fricke, A. Voigt, P. Veit, and K. Sundmacher (2015). Miniemulsion-based process for controlling the size and shape of zinc oxide nanoparticles. *Ind. Eng. Chem. Res.* **54**, 10293–10300. https://doi.org/10.1021/acs.iecr.5b01149.
82. V. R. V. Gopal and S. Kamila (2017). Effect of temperature on the morphology of ZnO nanoparticles: A comparative study. *Appl. Nanosci.* **7**, 75–82. https://doi.org/10.1007/s13204-017-0553-3.
83. K. Pushpanathan, S. Sathya, M. J. Chithra, S. Gowthami, and R. Santhi (2012). Influence of reaction temperature on crystal structure and band gap of ZnO nanoparticles. *Mater. Manuf. Process.* **27**, 1334–1342. https://doi.org/10.1080/10426914.2012.700163.
84. D. Das, B. C. Nath, P. Phukon, A. Kalita, and S. K. Dolui (2013). Synthesis of ZnO nanoparticles and evaluation of antioxidant and cytotoxic activity. *Colloids Surf. B* **111**, 556–560. https://doi.org/10.1016/j.colsurfb.2013.06.041.
85. T. S. Aldeen, H. E. A. Mohamed, and M. Maaza (2022). ZnO nanoparticles prepared via a green synthesis approach: Physical properties, photocatalytic and antibacterial activity. *J. Phys. Chem. Solids* **160**, 1–12. https://doi.org/10.1016/j.jpcs.2021.110313.
86. A. S. Bhosale, K. K. Abitkar, P. S. Sadalage, K. D. Pawar, and K. M. Garadkar (2021). Photocatalytic and antibacterial activities of ZnO nanoparticles synthesized by chemical method. *J. Mater. Sci: Mater. Electron.* **32**, 20510–20524. https://doi.org/10.1007/s10854-021-06563-5.
87. K. A. Nxumalo, J. O. Adeyemi, T. B. Leta, T. M. Pfukwa, S. N. Okafor, and O. A. Fawole (2024). Antifungal properties and molecular docking of ZnO NPs mediated using medicinal plant extracts. *Sci. Rep.* **14**, 18071. https://doi.org/10.1038/s41598-024-68979-3.
88. M. Wu, Z. Zhou, J. Yang, M. Zhang, F. Cai, and P. Lu (2021). ZnO nanoparticles stabilized oregano essential oil Pickering emulsion for functional cellulose nanofibrils packaging films with antimicrobial and antioxidant activity. *Int. J. Biol. Macromol.* **190**, 433–440. https://doi.org/10.1016/j.ijbiomac.2021.08.210.
89. A. S. Parlakyigit, C. Ergun, and O. Gokcekaya (2023). Synthesis of ZnO nanoparticles via spray atomization assisted inductively coupled plasma technique. *Ceram. Int.* **49**, 23035–23044. https://doi.org/10.1016/j.ceramint.2023.04.129.
90. M. Anbuvannan, M. Ramesh, G. Viruthagiri, N. Shanmugam, and N. Kannadasan (2015). Synthesis, characterization and photocatalytic activity of ZnO nanoparticles prepared by biological method. *Spectrochim. Acta A Mol. Biomol. Spectrosc.* **143**, 304–308. https://doi.org/10.1016/j.saa.2015.01.124.
91. A. Radhakrishnan, P. Rejani, J. S. Khan, and B. Beena (2016). Effect of annealing on the spectral and optical characteristics of nano ZnO: Evaluation of adsorption of toxic metal ions from industrial waste water. *Ecotoxicol. Environ. Saf.* **133**, 457–465. https://doi.org/10.1016/j.ecoenv.2016.08.001.
92. F. T. Thema, E. Manikandan, M. S. Dhlamini, and M. Maaza (2015). Green synthesis of ZnO nanoparticles via Agathosma betulina natural extract. *Mater. Lett.* **161**, 124–127. https://doi.org/10.1016/j.matlet.2015.08.052.
93. L. H. Zhao, R. Zhang, J. Zhang, and S. Q. Sun (2012). Synthesis and characterization of biocompatible ZnO nanoparticles. *Cryst. Eng. Comm.* **14**, 945–950. https://doi.org/10.1039/C1CE05621B.
94. C. Lizandara-Pueyo, S. Siroky, M. R. Wagner, A. Hoffmann, J. S. Reparaz, M. Lehmann, and Sebastian Polarz (2011). Shape anisotropy influencing functional properties: Trigonal prismatic ZnO nanoparticles as an example. *Adv. Funct. Mater.* **21**, 295–304. https://doi.org/10.1002/adfm.201000997.
95. S. S. Sharma, S. Palaty, and A. K. John (2020). Band gap modified zinc oxide nanoparticles: An efficient visible light active catalyst for wastewater treatment. *Int. J. Environ. Sci. Technol.* **18**, 1–14. https://doi.org/10.1007/s13762-020-02976-7.
96. S. Kumar and P. D. Sahare (2012). Observation of band gap and surface defects of ZnO nanoparticles synthesized via hydrothermal route at different reaction temperature. *Opt. Commun.* **285**, 5210–5216. https://doi.org/10.1016/j.optcom.2012.07.125.
97. N. Matinise, X. G. Fuku, K. Kaviyarasu, N. Mayedwa, and M. Maaza (2017). ZnO nanoparticles via Moringa oleifera green synthesis: Physical properties & mechanism of formation. *Appl. Surf. Sci.* **406**, 339–347. https://doi.org/10.1016/j.apsusc.2017.01.219.
98. H. M. Rietveld (1969). A profile refinement method for nuclear and magnetic structures. *J. Appl. Crystallogr.* **2**, 65–71. https://doi.org/10.1107/S0021889869006558.
99. D. A. A. Santos, A. D. P. Rocha, and M. A. Macêdo (2008). Rietveld refinement of transition metal doped ZnO. *Powder Diffr.* **23**, 36–41. https://doi.org/10.1154/1.2903739.
100. R. Yogamalar, R. Srinivasan, A. Vinu, K. Ariga, and A. C. Bose (2009). X-ray peak broadening analysis in ZnO nanoparticles. *Solid State Commun.* **149**, 1919–1923. https://doi.org/10.1016/j.ssc.2009.07.043.
101. S. B. Mullani, A. G. Dhodamani, A. Shellikeri, N. B. Mullani, A. K. Tawade, S. N. Tayade, J. Biscay, L. Dennany, and S. D. Delekar (2020). Structural refinement and electrochemical properties of one dimensional (ZnO NRs)1–x(CNs)x functional hybrids for serotonin sensing studies. *Sci. Rep.* **10**, 15955. https://doi.org/10.1038/s41598-020-72756-3.
102. F. I. H. Rhouma, F. Belkhiria, E. Bouzaiene, M. Daoudi, K. Taibi, J. Dhahri, and R. Chtourou (2019). The structure and photoluminescence of a ZnO phosphor synthesized by the sol gel method under praseodymium doping. *RSC Adv.* **9**, 5206–5217. https://doi.org/10.1039/c8ra09939a.
103. F. Pola-Albores, F. Paraguay-Delgado, Wilber Antunez-Flores, P. Amezaga-Madrid, E. Rios-Valdovinos, and M. Miki-Yoshida (2011). Microstructural study of ZnO nanostructures by rietveld analysis. *J. Nanomater.* **2011**, 643126. https://doi.org/10.1155/2011/643126.

104. P. Chand, A. Gaur, and A. Kumar (2012). Structural and optical properties of ZnO nanoparticles synthesized at different pH values. *J. Alloys Compd.* **539**, 174–178. https://doi.org/10.1016/j.jallcom.2012.05.104.
105. M. Wang, Y. Zhou, Y. Zhang, E. J. Kim, S. H. Hahn, and S. G. Seong (2012). Near-infrared photoluminescence from ZnO. *Appl. Phys. Lett.* **100**, 1–4. https://doi.org/10.1063/1.3692584.
106. M. A. Gondal, Q. A. Drmosh, Z. H. Yamani, and T. A. Saleh (2009). Synthesis of ZnO_2 nanoparticles by laser ablation in liquid and their annealing transformation into ZnO nanoparticles. *Appl. Surf. Sci.* **256**, 298–304. https://doi.org/10.1016/j.apsusc.2009.08.019.
107. J. E. Eixenberger, C. B. Anders, K. Wada, K. M. Reddy, R. J. Brown, J. Moreno-Ramirez, A. E. Weltner, C. Karthik, D. A. Tenne, D. Fologea, and D. G. Wingett (2019). Defect engineering of ZnO nanoparticles for bioimaging applications. *ACS Appl. Mater. Interfaces* **11**, 24933–24944. https://doi.org/10.1021/acsami.9b01582.
108. B. Manikandan, T. Endo, S. Kaneko, K. R. Murali, and R. John (2018). Properties of sol gel synthesized ZnO nanoparticles. *J. Mater. Sci. Mater. Electron.* **29**, 9474–9485. https://doi.org/10.1007/s10854-018-8981-8.
109. A. Sharma, B. P. Singh, S. Dhar, A. Gondorf, and M. Spasova (2012). Effect of surface groups on the luminescence property of ZnO nanoparticles synthesized by sol–gel route. *Surf. Sci.* **606**, 13–17. https://doi.org/10.1016/j.susc.2011.09.006.
110. M. Gusattia, G. S. Barroso, C. E. Maduro, D. A. Ribeiro, J. de Almeida, R. Bohn, C. Cardoso, L. Abreu, H. Gracher, and N. Cabral (2011). Effect of different precursors in the chemical synthesis of ZnO nanocrystals. *Mater. Res.* **14**, 264–267. https://doi.org/10.3390/inorganics10020016.
111. S. Cimitan, S. Albonetti, L. Forni, F. Peri, and D. Lazzari (2009). Solvothermal synthesis and properties control of doped ZnO nanoparticles. *J. Colloid Interface Sci.* **329**, 73–80. https://doi.org/10.1016/j.jcis.2008.09.060.
112. M. Ramani, S. Ponnusamy, C. Muthamizhchelvan, J. Cullen, S. Krishnamurthy, and E. Marsili (2013). Morphology-directed synthesis of ZnO nanostructures and their antibacterial activity. *Colloids Surf. B. Biointerfaces* **105**, 24–30. https://doi.org/10.1016/j.colsurfb.2012.12.056.
113. M. A. Ali, M. R. Idris, and M. E. Quayum (2013). Fabrication of ZnO nanoparticles by solution-combustion method for the photocatalytic degradation of organic dye. *J. Nanostructure Chem.* **3**, 1–6. https://doi.org/10.1186/2193-8865-3-36.
114. D. Raoufi (2013). Synthesis and microstructural properties of ZnO nanoparticles prepared by precipitation method. *Renew. Energy* **50**, 932–937. https://doi.org/10.1016/j.renene.2012.08.076.
115. N. Talebian, S. M. Amininezhad, and M. Doudi (2013). Controllable synthesis of ZnO nanoparticles and their morphology-dependent antibacterial and optical properties. *J. Photochem. Photobiol. B: Biol.* **120**, 66–73. https://doi.org/10.1016/j.jphotobiol.2013.01.004.
116. R. Saravanan, V. K. Gupta, V. Narayanan, and A. Stephen (2013). Comparative study on photocatalytic activity of ZnO prepared by different methods. *J. Mol. Liq.* **181**, 133–141. https://doi.org/10.1016/j.molliq.2013.02.023.
117. S. Sakohara, M. Ishida, and M. A. Anderson (1998). Visible luminescence and surface properties of nanosized ZnO colloids prepared by hydrolyzing zinc acetate. *J. Phys. Chem. B.* **102**, 10169–10175. https://doi.org/10.1021/jp982594m.
118. B. W. Chieng and Y. Y. Loo (2012). Synthesis of ZnO nanoparticles by modified polyol method. *Mater. Lett.* **73**, 78–82. https://doi.org/10.1016/j.matlet.2012.01.004.
119. S. S. Kurbanov, G. N. Panin, T. W. Kim, and T. W. Kang (2009). Strong violet luminescence from ZnO nanocrystals grown by the low-temperature chemical solution deposition. *J. Lumin.* **129**, 1099–1104. https://doi.org/10.1016/j.jlumin.2009.05.005.
120. W. Water, T. H. Fang, L. W. Ji, and C. C. Lee (2009). Effect of growth temperature on photoluminescence and piezoelectric characteristics of ZnO nanowires. *Mater. Sci. Eng. B* **158**, 75–78. https://doi.org/10.1016/j.mseb.2009.01.021.
121. S. Klubnuan, S. Suwanboon, and P. Amornpitoksuk (2016). Effects of optical band gap energy, band tail energy and particle shape on photocatalytic activities of different ZnO nanostructures prepared by a hydrothermal method. *Opt. Mater.* **53**, 134–141. https://doi.org/10.1016/j.optmat.2016.01.045.
122. R. Raji and K. G. Gopchandran (2017). ZnO nanostructures with tunable visible luminescence: Effects of kinetics of chemical reduction and annealing. *J. Sci. Adv. Mater. Devices* **2**, 51–58. https://doi.org/10.1016/j.jsamd.2017.02.002.
123. S. Agarwal, L. Jangir, K. S. Rathore, M. Kumar, and K. Awasthi (2019). Morphology-dependent structural and optical properties of ZnO nanostructures. *Appl. Phys. A* **125**, 553. https://doi.org/10.1007/s00339-019-2852-x.
124. J. Duraimurugan, G. S. Kumar, and M. V. P. Maadeswaran (2018). Morphology and size controlled synthesis of zinc oxide nanostructures and their optical properties. *J. Mater. Sci. Mater. Electron.* **29**, 9339–9346. https://doi.org/10.1007/s10854-018-8964-9.
125. E. G. Goh, X. Xu, and P. G. McCormick (2014). Effect of particle size on the UV absorbance of zinc oxide nanoparticles. *Scr. Mater.* **78–79**, 49–52. https://doi.org/10.1016/j.scriptamat.2014.01.033.
126. H. Rai, Ch. Prashant, and N. Kondal (2022). A review on defect related emissions in undoped ZnO nanostructures. *Mater. Today Proc.* **48**, 1320–1324. https://doi.org/10.1016/j.matpr.2021.08.343.
127. B. X. Lin, Z. X. Fu, and Y. B. Jia (2001). Green luminescent center in undoped zinc oxide films deposited on silicon substrates. *Appl. Phys. Lett.* **79**, 943–945. https://doi.org/10.1063/1.1394173.
128. A. Dey, P. G. Ray, S. Dhara, and S. Neogi (2022). Optically engineered ZnO nanoparticles: Excitable at visible wavelength and lowered cytotoxicity towards bioimaging applications. *Appl. Surf. Sci.* **592**, 1–12. https://doi.org/10.1016/j.apsusc.2022.153303.
129. M. Sathya and K. Pushpanathan (2018). Synthesis and optical properties of Pb doped ZnO nanoparticles. *Appl. Surf. Sci.* **449**, 346–357. https://doi.org/10.1016/j.apsusc.2017.11.127.
130. K. S. Babun, A. R. Reddy, Ch. Sujatha, and K. V. Redd (2013). Optimization of UV emission intensity of ZnO nanoparticles by changing the excitation wavelength. *Mater. Lett.* **99**, 97–100. https://doi.org/10.1016/j.matlet.2013.02.079.
131. S. K. Mishra, R. K. Srivastava, and S. G. Prakash (2012). ZnO nanoparticles: Structural, optical and photoconductivity characteristics. *J. Alloys Compd.* **539**, 1–6. https://doi.org/10.1016/j.jallcom.2012.06.024.
132. X. Lu, K. Wu, H. Wu, W. Cao, Q. Zhu, J. Zhou, and Y. Zhang (2023). Near-infrared photoluminescence radiation from the interface of an annealed ZnO nano thin film/silicon heterostructure array. *Opt. Mater.* **137**, 1–8. https://doi.org/10.1016/j.optmat.2023.113549.
133. T. Andelman, Y. Gong, M. Polking, M. Yin, I. Kuskovsky, G. Neumark, and S. O'Brien (2005). Morphological control and photoluminescence of zinc oxide nanocrystals. *J. Phys. Chem. B.* **109**, 14314–14318. https://doi.org/10.1021/jp050540o.
134. R. D. Yang, S. Tripathy, Y. Li, and H. J. Sue (2005). Photoluminescence and micro-Raman scattering in ZnO nanoparticles: The influence of acetate adsorption. *Chem. Phys. Lett.* **411**, 150–154. https://doi.org/10.1016/j.cplett.2005.05.125.

135. J. Haque, M. Bellah, R. Hassan, and S. Rahman (2020). Synthesis of ZnO nanoparticles by two different methods & comparison of their structural, antibacterial, photocatalytic and optical properties. *NanoExpress* **1**, 010007. https://doi.org/10.1088/2632-959X/ab7a43.
136. R. Bekkar, L. Laânab, D. Boyer, R. Mahiou, and B. Jaber (2017). Influence of the sol gel synthesis parameters on the photoluminescence properties of ZnO nanoparticles. *Mater. Sci. Semicond. Process.* **71**, 181–187. https://doi.org/10.1016/j.mssp.2017.07.027.
137. K. P. Raj and K. Sadayandi (2016). Effect of temperature on structural, optical and photoluminescence studies on ZnO nanoparticles synthesized by the standard co-precipitation method. *Physica B Condens. Matter* **487**, 1–7. https://doi.org/10.1016/j.physb.2016.01.020.
138. T. P. Rao, G. K. Goswami, and K. K. Nanda (2014). Detailed understanding of the excitation-intensity dependent photoluminescence of ZnO materials: Role of defects. *J. Appl. Phys.* **115** (213513), 1–8. https://doi.org/10.1063/1.4881779.
139. Z. Qiu, B. Hao, X. Gu, Z. Wang, N. Xie, J. W. Y. Lam, H. Hao, and B. Z. Tang (2018). A general powder dusting method for latent fingerprint development based on AIEgens. *Sci. China Chem.* **61**, 966–970. https://doi.org/10.1007/s11426-018-9280-1.
140. V. Divya, B. Agrawal, A. Srivastav, P. Bhatt, S. Bhowmik, Y. K. Agrawal, and P. Maity (2018). Fluorescent amphiphilic silica nanopowder for developing latent fingerprints. *Aust. J. Forensic Sci.* **52**, 1–14. https://doi.org/10.1080/00450618.2018.1533036.
141. R. Hartzell-Baguley, E. Hipp, N. R. Morgan, and S. L. Morgan (2007). Chemical composition of latent fingerprints by gas chromatography-mass spectrometry an experiment for an instrumental analysis course. *J. Chem. Educ.* **84**, 689–691. https://doi.org/10.1021/ed084p689.
142. R. S. Croxton, M. G. Baron, D. Butler, T. Kentc, and V. G. Sears (2010). Variation in amino acid and lipid composition of latent fingerprints. *Forensic Sci. Int.* **199**, 93–102. https://doi.org/10.1016/j.forsciint.2010.03.019.
143. P. Fritz, W. van Bronswjik, K. Lepkova, S. W. Lewis, K. F. Lim, D. E. Martin, and L. Puskar (2013). Infrared microscopy studies of the chemical composition of latent fingermark residues. *Microchem. J.* **111**, 40–46. https://doi.org/10.1016/j.microc.2012.08.005.
144. Y. Li, X. Hu, H. Yao, Y. Ye, and J. Zhou (2023). Development of latent fingerprints by degradable highly-adhering powder-a long-term strategy for the fading of fingerprint residues. *Dyes Pigm.* **219**, 1–8. https://doi.org/10.1016/j.dyepig.2023.111597.
145. A. Girod, R. Ramotowski, and C. Weyermann (2012). Composition of fingermark residue: A qualitative and quantitative review. *Forensic Sci. Int.* **223**, 10–24. https://doi.org/10.1016/j.forsciint.2012.05.018.
146. T. Atherton, R. Croxton, M. Baron, J. Gonzalez-Rodriguez, L. Gámiz-Gracia, and A. M. García-Campaña (2012). Analysis of amino acids in latent fingerprint residue by capillary electrophoresis-mass spectrometry. *J. Sep. Sci.* **35**, 2994–2999. https://doi.org/10.1002/jssc.201200398.
147. N. E. Archer, Y. Charles, J. A. Elliott, and S. Jickells (2005). Changes in the lipid composition of latent fingerprint residue with time after deposition on a surface. *Forensic Sci. Int.* **154**, 224–239. https://doi.org/10.1016/j.forsciint.2004.09.120.
148. P. Joshi, V. Shewale, R. Pandey, V. Shanker, S. Hussain, and S. P. Karna (2011). Site specific interaction between ZnO nanoparticles and tryptophan: A first principles quantum mechanical study. *Phys. Chem. Chem. Phys.* **13**, 476–479. https://doi.org/10.1039/c0cp01466d.
149. G. Nawrocki and M. Cieplak (2013). Amino acids and proteins at ZnO–water interfaces in molecular dynamics simulations. *Phys. Chem. Chem. Phys.* **15**, 13628–13636. https://doi.org/10.1039/C3CP52198B.
150. P. S. Maddahi, M. Yeganeh, and F. B. Baghsiyahi (2019). ZnO nanoparticles as a sensitive platform for detection of nitration in tyrosine and tryptophan: A DFT study. *Mater. Chem. Phys.* **237**, 1–8. https://doi.org/10.1016/j.matchemphys.2019.121857.
151. M. J. Limo and C. C. Perry (2015). Thermodynamic study of interactions between ZnO and ZnO binding peptides using isothermal titration calorimetry. *Langmuir* **31**, 6814–6822. https://doi.org/10.1021/acs.langmuir.5b01347.
152. T. H. Do, V. T. Nguyen, Q. D. Nguyen, M. N. Chu, T. C. Q. Ngo, and L. V. Tan (2020). Equilibrium. Kinetic and thermodynamic studies for sorption of phosphate from aqueous solutions using ZnO nanoparticles. *Processes* **8**, 1–19. https://doi.org/10.3390/pr8111397.
153. J. Zou, X. Wang, C. Xiong, J. Wu, F. Zhang, and Z. Mao (2024). Enhanced fluorescence imaging of level 1–3 latent fingerprints on multi-materials through lipophilicity-tunable probes. *Sens. Actuators B. Chem.* **417**, 1–8. https://doi.org/10.1016/j.snb.2024.136154.
154. H. Chen, R. Ma, and M. Zhang (2022). Recent progress in visualization and analysis of fingerprint level 3 features. *ChemistryOpen* **11**, 1–19. https://doi.org/10.1002/open.202200091.
155. N. Zaeri, Chapter 3—Minutiae-based fingerprint extraction and recognition, in J. Yang (ed.), *Biometrics* (IntechOpen Limited, London, 2011), pp. 55–78. https://doi.org/10.5772/17527.
156. K. Abhishek and A. Yogi (2015). A minutiae count based method for fake fingerprint detection. *Procedia Comput. Sci.* **58**, 447–452. https://doi.org/10.1016/j.procs.2015.08.061.
157. K. N. Win, K. Li, J. Chen, P. F. Viger, and K. Li (2019). Fingerprint classification and identification algorithms for criminal investigation: A survey. *Future Gener. Comput. Syst.* **110**, 758–771. https://doi.org/10.1016/j.future.2019.10.019.
158. M. Algarra, K. Radotić, A. Kalauzi, D. Dragosav Mutavžić, A. Savić, J. Jiménez-Jiménez, E. Rodríguez-Castellón, J. C. G. Esteves da Silva, and J. J. Guerrero-González (2014). Fingerprint detection and using intercalated CdSe nanoparticles on non-porous surfaces. *Anal. Chim. Acta* **812**, 228–235. https://doi.org/10.1016/j.aca.2014.01.015.
159. G. Dutta and A. Sugumaran (2021). Bioengineered zinc oxide nanoparticles: Chemical, green, biological fabrication methods and its potential biomedical applications. *J. Drug Deliv. Sci. Technol.* **66**, 102853. https://doi.org/10.1016/j.jddst.2021.102853.
160. S. Sadhasivam, M. Shanmugam, P. D. Umamaheswaran, A. Venkattappan, and A. Shanmugam (2021). Zinc oxide nanoparticles: Green synthesis and biomedical applications. *J. Clust. Sci.* **32**, 1441–1455. https://doi.org/10.1007/s10876-020-01918-0.
161. A. K. Mandal, S. Katuwal, F. Tettey, A. Gupta, S. Bhattarai, S. Jaisi, D. P. Bhandari, A. K. Shah, N. Bhattarai, and N. Parajuli (2022). Current research on zinc oxide nanoparticles: Synthesis, characterization, and biomedical applications. *Nanomaterials* **12**, 3066. https://doi.org/10.3390/nano12173066.
162. N. K. Jain and M. Tailang (2023). Green synthesis of zinc oxide nanoparticles and their biomedical applications in cancer treatment: Current status and future perspectives. *Appl. Nanosci.* **13**, 6605–6629. https://doi.org/10.1007/s13204-023-02946-8.
163. E. Bilensoy and C. Varan (2023). Is there a niche for zinc oxide nanoparticles in future drug discovery? *Expert Opin. Drug Discov.* **18**, 943–945. https://doi.org/10.1080/17460441.2023.2230152.
164. B. S. Shashikala, H. B. Premkumar, G. P. Darshan, H. Nagabhushana, S. C. Sharma, and S. C. Prashantha (2019). Rational design of bi-functional RE^{3+} (RE=Tb, Ce) and alkali metals

(M^+=Li, Na, K) co-doped $CaAl_2O_4$ nanophosphors for solid state lighting and advanced forensic applications. *Mater. Res. Bull.* **115**, 88–97. https://doi.org/10.1016/j.materresbull.2019.03.002.
165. C. V. Prasad, L. Prasad, S. Lukose, and P. Agarwal (2021). Latent fingerprint development by using silver nanoparticles and silver nitrate—A comparative study. *J. Forensic. Sci.* **66**, 1065–1074. https://doi.org/10.1111/1556-4029.14664.
166. B. R. R. Krushna, H. H. Chiu, M. K. Ho, T. E. Hsu, B. L. Lyu, W. C. Lo, B. Subramanian, K. Manjunatha, S. Yun Wu, and H. Nagabhushana (2024). Investigating Fe-doped yttrium oxide nanophosphors for enhanced latent fingerprint visualization and deep learning analysis. *Mater. Today Sustain.* **25** (100629), 1–22. https://doi.org/10.1016/j.mtsust.2023.100629.
167. Z. Wang, X. Jiang, W. Liu, G. Lu, and X. Huang (2019). A rapid and operator-safe powder approach for latent fingerprint detection using hydrophilic Fe_3O_4@SiO_2-CdTe nanoparticles. *Sci. China Chem.* **62**, 889–896. https://doi.org/10.1007/s11426-019-9460-0.
168. A. S. Solomon and P. Vasudevan (2023). BiOCl: Dy^{3+}/Ba^{2+} nanophosphors: Synthesis, luminescence characteristics and applications in latent fingerprint detection and cheiloscopy. *J Photochem. Photobiol. A Chem.* **442** (114767), 1–12. https://doi.org/10.1016/j.jphotochem.2023.114767.
169. X. Ren, D. Chen, X. Meng, F. Tang, X. Hou, D. Han, and L. Zhang (2009). Zinc oxide nanoparticles/glucose oxidase photoelectrochemical system for the fabrication of biosensor. *J. Colloid Interface Sci.* **334**, 183–187. https://doi.org/10.1016/j.jcis.2009.02.043.
170. J. Wan, L. Chen, W. Li, S. Cui, and B. Yuan (2022). Preparation of novel magnetic nanomaterials based on facile coprecipitation for developing latent fingerprints (LFP) in crime scenes. *ACS Omega* **7**, 1712–1721. https://doi.org/10.1021/acsomega.1c04208.
171. J. Rodrigues, S. O. Pereira, J. Zanoni, C. Rodrigues, M. Brás, F. M. Costa, and T. Z. Monteiro (2022). ZnO Transducers for photoluminescence-based biosensors: A review. *Chemosensors* **10**, 39. https://doi.org/10.3390/chemosensors10020039.
172. A. Umar, M. M. Rahman, M. Vaseem, and Y. B. Hahn (2019). Ultra-sensitive cholesterol biosensor based on low-temperature grown ZnO nanoparticles. *Electrochem. Commun.* **11**, 118–121. https://doi.org/10.1016/j.elecom.2008.10.046.
173. N. Tripathy and D. H. Kim (2018). Metal oxide modified ZnO nanomaterials for biosensor applications. *Nano Converg.* **5**, 27. https://doi.org/10.1186/s40580-018-0159-9.
174. A. Arshad, M. A. Farrukh, S. Ali, M. Khaleeq-ur-Rahman, and M. A. Tahir (2015). Development of latent fingermarks on various surfaces using ZnO-SiO_2 nanopowder. *J. Forensic Sci.* **60**, 1182–1187. https://doi.org/10.1111/1556-4029.12890.
175. A. Becue, C. Champod, and P. Margot (2007). Use of gold nanoparticles as molecular intermediates for the detection of fingermarks. *Forensic Sci. Int.* **168**, 169–176. https://doi.org/10.1016/j.forsciint.2006.07.014.
176. F. Haque, A. D. Westland, J. Milligan, and F. M. Kerr (1989). A small particle (iron oxide) suspension for detection of latent fingerprints on smooth surfaces. *Forensic Sci. Int.* **41**, 73–82. https://doi.org/10.1016/0379-0738(89)90238-7.
177. M. Sametband, I. Shweky, U. Banin, D. Mandler, and J. Almog (2007). Application of nanoparticles for the enhancement of latent fingerprints. *Chem. Commun.* **11**, 1142–1144. https://doi.org/10.1039/b618966k.
178. H. W. Tang, W. Lu, C. M. Che, and K. M. Ng (2010). Gold nanoparticles and imaging mass spectrometry: Double imaging of latent fingerprints. *Anal. Chem.* **82**, 1589–1593. https://doi.org/10.1021/ac9026077.
179. D. Gao, F. Li, J. Song, X. Xu, Q. Zhang, and L. Niu (2009). One step to detect the latent fingermarks with gold nanoparticles. *Talanta* **80**, 479–483. https://doi.org/10.1016/j.talanta.2009.07.007.
180. P. L. T. Lee, F. K. Kanodarwala, C. Lennard, X. Spindler, V. Spikmans, C. Roux, and S. Moret (2019). Latent fingermark detection using functionalised silicon oxide nanoparticles: Method optimisation and evaluation. *Forensic Sci. Int.* **298**, 372–383. https://doi.org/10.1016/j.forsciint.2019.02.038.
181. A. Sharma, A. Agrawal, S. Kumar, K. K. Awasthi, K. Awasthi, and A. Awasthi, Chapter 23—Zinc oxide nanostructures–based biosensors, in K. Awasthi (ed.), *Nanostructured Zinc Oxide: Synthesis, Properties and Applications Metal Oxides* (Elsevier, Amsterdam, 2021), pp. 655–695. https://doi.org/10.1016/B978-0-12-818900-9.00002-4.